12-2021

Molecular Dynamics Study of Atomic Diffusion in Cantor High Entropy Alloy in the Selective Laser Melting Process

Mathew Z. Farias
The University of Texas Rio Grande Valley

MOLECULAR DYNAMICS STUDY OF ATOMIC DIFFUSION IN CANTOR HIGH ENTROPY ALLOY IN THE SELECTIVE LASER MELTING PROCESS

A Thesis

by

MATHEW Z. FARIAS

Submitted in Partial Fulfillment of the

Requirements for the Degree of

MASTER OF SCIENCE IN ENGINEERING

Major Subject: Manufacturing Engineering

The University of Rio Grande Valley

December 2021

MOLECULAR DYNAMICS STUDY OF ATOMIC DIFFUSION IN CANTOR HIGH ENTROPY ALLOY IN THE SELECTIVE LASER MELTING PROCESS

A Thesis

by

MATHEW Z. FARIAS

COMMITTEE MEMBERS

Dr. Jianzhi Li

Chair of Committee

Dr. Ben Xu (Mississippi State University)

Co-Chair of Committee

Dr. Shanshan Zhang

Committee Member

Dr. Farid Ahmed

Committee Member

December 2021

ABSTRACT

Farias, Mathew Z., Molecular Dynamics Study of Atomic Diffusion in Cantor High Entropy Alloy in the Selective Laser Melting Process. Master of Science in Engineering (MSE), December 2021, 72 pp., 26 figures, 5 tables, 57 references.

High entropy alloys (HEAs) are compositionally complex alloys that are comprised of 5 or more principle elements at near equimolar concentrations. The Selective Laser Melting (SLM) method generally melts pure elemental powders or prefabricated alloy powders, this process allows for the production of heterogeneous structures that would be difficult to create through more conventional means. *In-situ* alloying in SLM, or Laser Additive Alloying (LAA), using pure elemental powders is a promising means of producing what would otherwise be costly and difficult to fabricate products with less defects using prefabricated powders, therefore this new approach could enable the ability to further tailor alloys and reduce the energy consumption by utilizing the exothermic alloy reaction. However, the effect of the atomic diffusion of elements in the molten pool on the formation of HEA remains poorly understood. In this study, the well-discussed Cantor HEA (Co-Cr-Mn-Ni-Fe) was numerically studied in an *in-situ* alloying situation, where pure elemental powders (Co, Cr, Mn, Ni, Fe) distributed on a powder bed were melted by a laser, modeled by a moving volume depositing energy, and was subsequently allowed to quench back to the room temperature. The diffusion of specific elements, with respect to their original clusters, was tracked via Mean Square Displacement (MSD) as well as the final

composition of key locations. Moreover, Young's modulus, shear modulus, and lattice thermal conductivity coefficient were simulated and compared with published experimental works. Lastly, the diffusion coefficients were calculated in 3 near-equimolar alloys and 3 alloys with various Fe weight percentages to study the effects of entropy on the tracer diffusion rates. The findings in this study in terms of diffusion behavior can assist the design and manufacturing of other novel HEAs for applications in extreme environment.

DEDICATION

I dedicate this thesis to my family, to which without their support and constant encouragement, I would probably never have made it so far.

ACKNOWLEDGMENTS

I would like to thank Dr. Jianzhi Li for his support through the program making it possible for me to focus entirely on my studies and my research. I'd also like to give special thanks to Dr. Ben Xu, his constant mentorship over the last two years has helped me grow immensely as both a person and researcher. I would like to extend special thanks to Dr. Han Hu from the University of Arkansas for sharing a rapid introduction to Molecular Dynamics, without his early support this thesis would not have been possible. I'd like to extend my appreciation to Dr. Farid Ahmed and Dr. Shanshan Zhang for meeting constantly with me throughout my graduate degree and offering their expert insights into my work and helping me refine this thesis. I'd also like to thank to all the members of the MTL and SLM research teams, especially Lazaro Lopez and Joni Chandra Dhar who collaborated with me extensively to help me acclimate to the research environment at the start of my graduate studies. I would also like to thank my best friend Samantha Gonzalez, a fellow graduate student who shared many panicked and stressful occasions with me over the last two years. Finally, this work used the Extreme Science and Engineering Discovery Environment (XSEDE) Stampede2 at TACC through allocation TG-CTS200013 and Bridges2 at PSC through allocation TG-MCH200010, supported by National Science Foundation grant number ACI-1548562.

TABLE OF CONTENTS

Page

ABSTRACT iii

DEDICATION v

ACKNOWLEDGMENTS vi

TABLE OF CONTENTS vii

LIST OF TABLES x

LIST OF FIGURES xi

CHAPTER I 1

1.1 Background and Motivation 1

1.2 High Entropy Alloy “core effects” 2

1.3 Fabrication of HEA 8

1.4 Knowledge Gap 11

1.5 Research Questions and Hypothesis 11

CHAPTER II 13

2.1 Diffusion and Diffusion Coefficients 13

2.1.1 Fick’s Laws of Diffusion 13

2.1.2 Interdiffusion 15

2.1.3 Tracer and Self Diffusion 17

2.1.4 Molecular Dynamics Study of Diffusion Coefficients 17

CHAPTER III 20

3.1 Methodology and Simulation Setup of the Powder Bed 20

3.2 Methodology and Simulation Setup for Young's Modulus and Lattice Thermal Conductivity 23

3.3 Simulation of Diffusion Coefficients 26

3.4 Computational Resources and Acknowledgment 28

CHAPTER IV 29

4.1 Single-track Studies 29

4.1.1 Study of laser energy density and diffusion 29

4.1.2 Energy density and composition in single track study 34

4.1.3 Crystal Structure of Single-Track Studies 36

4.2 Multiple laser track study 37

4.2.1 Multiple Track Study and diffusion 37

4.2.2 Multiple Track Study Composition 39

4.2.3 Crystallization of Powder Bed 41

4.2.4 Simulation of Lattice Thermal Conductivity and Young's Modulus 41

4.3 Diffusion and Entropy 43

CHAPTER V 47

REFERENCES 49

APPENDIX A 56

BIOGRAPHICAL SKETCH 72

LIST OF TABLES

Page

Table 1 Crystal Lattice Parameters for Fe, Co, Cr, Ni..... 21

Table 2 Laser Parameters for Single Track Study..... 22

Table 3 Average Diffusion Coefficient..... 33

Table 4: Young's Modulus, Shear Modulus, Poisson's Ratio..... 43

Table 5 Diffusion Coefficients and Varying Configuration Entropy..... 45

LIST OF FIGURES

Page

Figure 1 High Entropy Materials Applications (Ma et al., 2021) 2

Figure 2: Severe Lattice Distortion represented in AlCrNiCoTi HEA (Kao et al., 2009) 3

Figure 3: Hardness of HEA with increasing Al content, and phases represented (Yeh et al., 2004) 4

Figure 4: Effects of increasing Al content on phase and material hardness of CoCrFeNi Alloy (Kao et al., 2009) 5

Figure 5: Stress-Strain Curves of CoCrFeNi-Nbx Alloys (Liu et al., 2015) 6

Figure 6: Arrhenius Plots for Diffusion Coefficients in a CoCrFeMnNi system from Tsai et al. (Tsai et al., 2013) 7

Figure 7: Lattice Potential Energy from Tsai et al. (Tsai et al., 2013) 8

Figure 8 Schematic of Vacuum Arc Melting Chamber (Stansbury & Buchanan, 2000) 9

Figure 9 Demonstration of Selective Laser Melting Concept (Ahmed & Mian, 2019) 10

Figure 10: infinitesimal control volume, where Jy represents the flux moving in the Y direction (Mehrer, 2007) 14

Figure 11 Molecular Dynamics Breakdown (Grigera, 2005) 18

Figure 12 (a) isometric preview of powder bed model used in MD study (b) top-down perspective of powder bed model, red circle indicates approximate dimensions and start location of the laser. Powders are colored accordingly: green is Mn, yellow is Ni, blue is Cr, ... 22

Figure 13 Time series of powder bed with a 0.06 nm/ps laser scan speed over 200 ps 29
Figure 14 Powders selected for study, atoms in these regions were also studied independently . 31
Figure 15 Mean Square Displacements of atoms selected a group based on what particle it was a constituent under a laser with scanning speed (a) 0.060 nm/ps and (b) 0.030 nm/ps. 32
Figure 16 Pixel overlays of the powder bed under three different scanning speeds (a) 0.060 nm/ps; (b) 0.045 nm/ps, and (c) 0.030 nm/ps, respectively..... 34
Figure 17 Composition of the area indicated in Fig. 15c..... 36
Figure 18 Polyhedral Template Matching (PTM) Analysis of solidified powder bed after (a) 0.06 nm/ps (b) 0.045 nm/ps, (c) 0.03 nm/ps scanning speeds..... 37
Figure 19 Initial powder bed configuration and laser pathing. 38
Figure 20 Mean Square Displacements of atoms selected under two subsequent tracks traveling 0.03 nm/ps 39
Figure 21 Pixel overlay of 2-track simulation using a meander hatch strategy. 39
Figure 22 composition of the area indicated in fig. 21 40
Figure 23 PTM Analysis of solidified powder bed after 2 track meander scan 41
Figure 24 Lattice Thermal Conductivity of CoCrMnNiFe at 4 given temperatures..... 42
Figure 25 Diffusion Coefficients compared to Configurational Entropy, this comparison is done by comparing the alloys of increasing Fe content while maintaining equimolarity between the remaining 4 elements, proportions given in atomic percentage. 44
Figure 26 Diffusion Coefficients as compared to the number of components in an alloy, This study maintained equimolar ratios between the constituent elements while removing elements in each step 46

CHAPTER I

INTRODUCTION

1.1 Background and Motivation

High entropy alloys (HEAs) are composed of 5 or more principal components at near equal atomic composition (Zhang et al., 2014). The name HEA was first coined by Yeh *et al.* (Yeh et al., 2004), the subset of alloys would be also simultaneously referred to as multi-component alloys by Cantor *et al.* (Cantor *et al*., 2004). HEA can exhibit exemplary material properties, such as high wear resistance (Chuang *et al*., 2011), high-temperature strength (Senkov *et al*., 2011), high hardness (Sha *et al*., 2020), and corrosion resistance depending (Chou *et al*., 2010) on what constituent element the system is made of and its crystal structure (Tsai, 2013; Zhang *et al*., 2014), many studies attribute these properties to the hypothesis of high lattice distortion exhibited in such alloys (Miracle & Senkov, 2017; Pickering *et al*., 2016).

HEA represents a new frontier in alloy development, one large component to be explained in Section 1.2, is the theory of "cocktail effects"; the "cocktail effect" theory suggests that HEA can be further tailored by small changes of composition for a wide variety of extreme applications, possibilities ranging from the aerospace, nuclear, renewable energy applications, as shown in Fig. 1. Beyond metallic HEAs, the option of High Entropy Materials such as borides, and oxides, are of great interest for even broader applications (Ma *et al*., 2021). The Cantor

HEA, Co-Cr-Mn-Ni-Fe, has been studied the most and is known to create a single disordered solid solution with an FCC crystal structure (Choi *et al*., 2018), due to the abundance of experimental literature related to the Cantor HEA it has been chosen as a suitable alloy to study through means of simulation and will be the focus alloy in this paper.

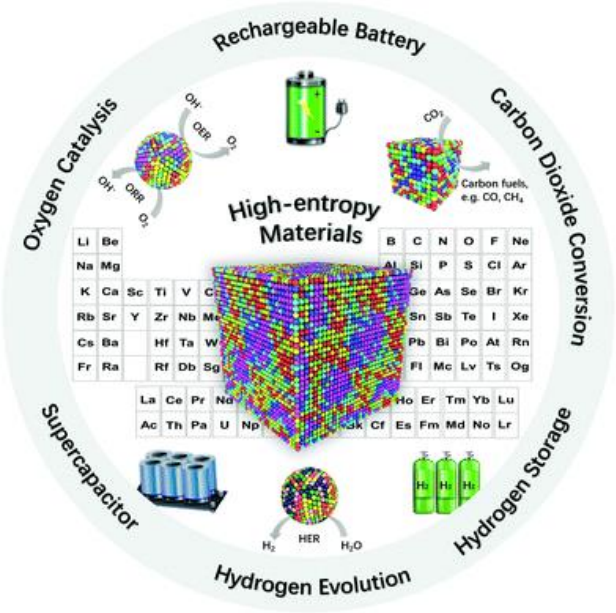

Figure 1 High Entropy Materials Applications (Ma et al., 2021)

1.2 High Entropy Alloy "core effects"

Shortly after discovery, Yeh classified 4 core effects (Yeh *et al*., 2004) to HEA, many of which have been debated, the following section will discuss some literature on each of the effects.

- High Entropy Effect

The High Entropy effect in HEA refers to the high mixing entropy involved in the system and is largely believed to inhibit the formation of competing stoichiometric compounds or competing phases (Gao *et al*., 2016;Yang *et al*., 2012; Zhang *et al*., 2011), it is believed that

with a low size difference between atoms, δ, lower mixing enthalpy, and high mixing entropy there is a more significant chance for a disordered solid solution to form.

- Severe Lattice Distortion

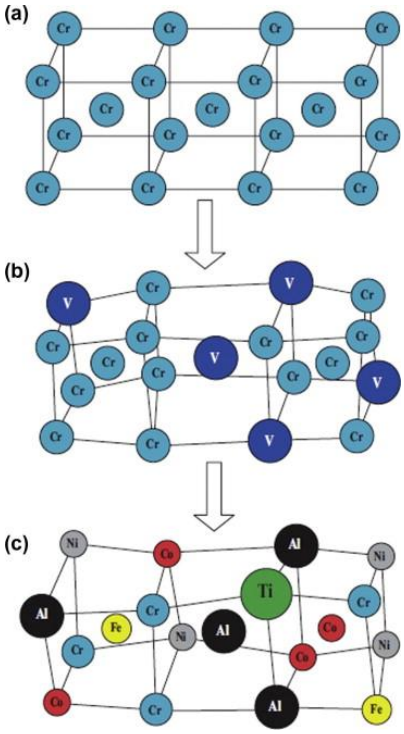

Figure 2: Severe Lattice Distortion represented in AlCrNiCoTi HEA (Kao et al., 2009)

In an HEA there are many constituent elements with no clear solvent element, as such it typically occurs that any element may occupy any lattice site, resulting in high lattice distortion; a depiction of this effect can be seen in Fig. 2. Whereas in the traditional alloy, trace additives cause some distortion due to their atomic radii and electric potentials, in HEAs the issue is exacerbated and was initially believed to contribute to slower kinetics and higher tensile strength. Typically BCC and FCC crystal structures have been observed in HEAs, wherein it is theorized that the extreme lattice distortion may attribute to the tensile brittle behavior and high strengths of BCC structure HEAs (Yeh *et al.*, 2004).

- Cocktail effects

Cocktail effects are a term used to describe the effects of mixing many elements in a single alloy and the effects of adding trace elements to mechanical properties. This may be due to the lattice distortion; this can be seen in work published by Yeh *et al*. (Yeh *et al*., 2004) in a HEA comprised of CuCoNiCrFe and a trace amount of Al. As the Al concentration increased, to a maximum of about 3 at%, the structure of the originally FCC HEA shifted to a BCC structure this is significant because the BCC structure HEA exhibits higher hardness' and high ultimate strength although they typically sacrifice ductility for these properties. As seen in Fig. 3, after the composition in the HEA is about 0.5 at% Al the alloy begins to show the presence of both an FCC and BCC phase, during which the hardness of the alloy increases dramatically.

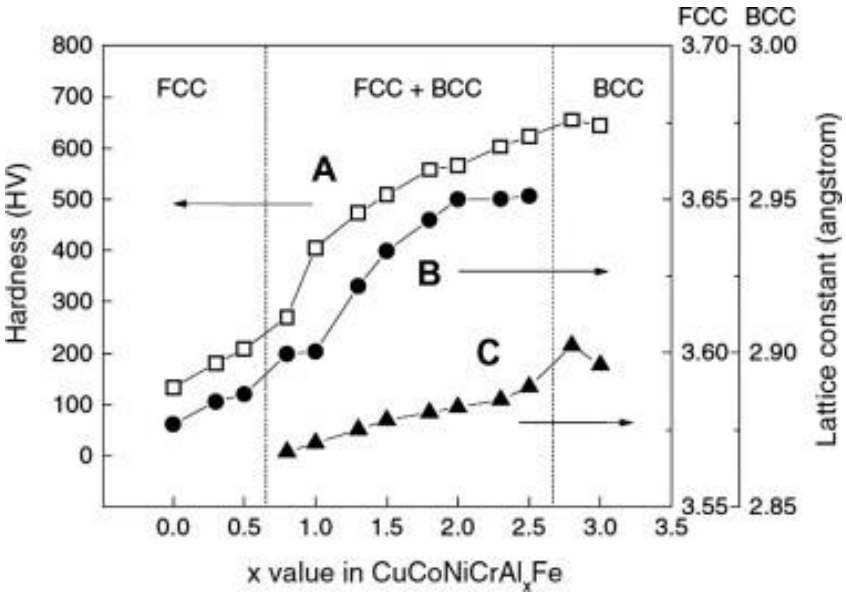

Figure 3: Hardness of HEA with increasing Al content, and phases represented (Yeh et al., 2004)

Removal of key elements from the HEA dramatically changes the results as seen by work recorded by Kao *et al.* (2009). A similar alloy was prepared to omit the use of copper in a CoNiCrFe-Alx alloy, the authors still considered this a HEA as it appeared to exhibit behavior

seen in HEAs, it was seen that the initial FCC hardness was similar to the 5 component HEA however upon the addition of Al the alloy began to transition, the maximum hardness was only capable of reaching just passed 500 Hv compared to that of the ~650 Hv hardness in the 5 component HEA, the FCC to BCC change as well as change in hardness can be seen Fig. 4.

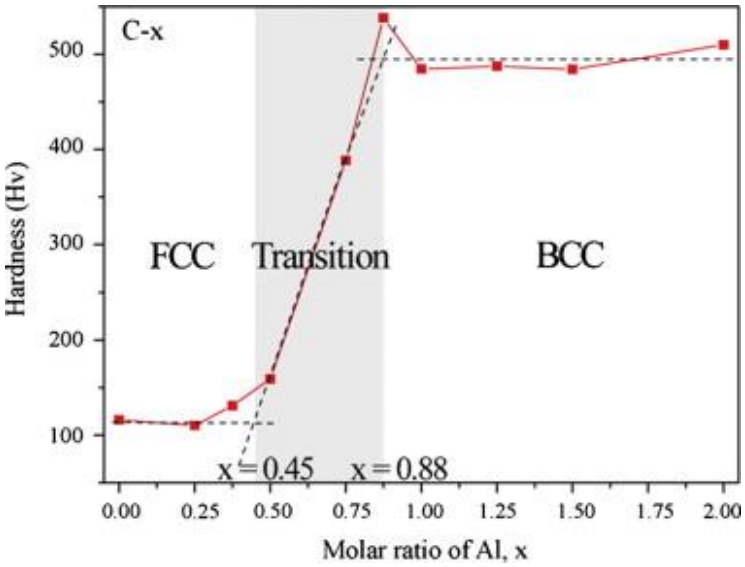

Figure 4: Effects of increasing Al content on phase and material hardness of CoCrFeNi Alloy (Kao et al., 2009)

It has been noted that the cocktail effect can have extreme effects on material properties and by simply adjusting elemental concentrations HEAs can be customized for a variety of purposes. Fig. 5 shows the effects of adding niobium in trace amounts to a CoCrFeNi alloy the results found that by increasing the niobium concentration one could increase the ultimate tensile stress of the alloy but noted that the materials saw a drastic loss of plasticity as a result. (Liu *et al.*, 2015)

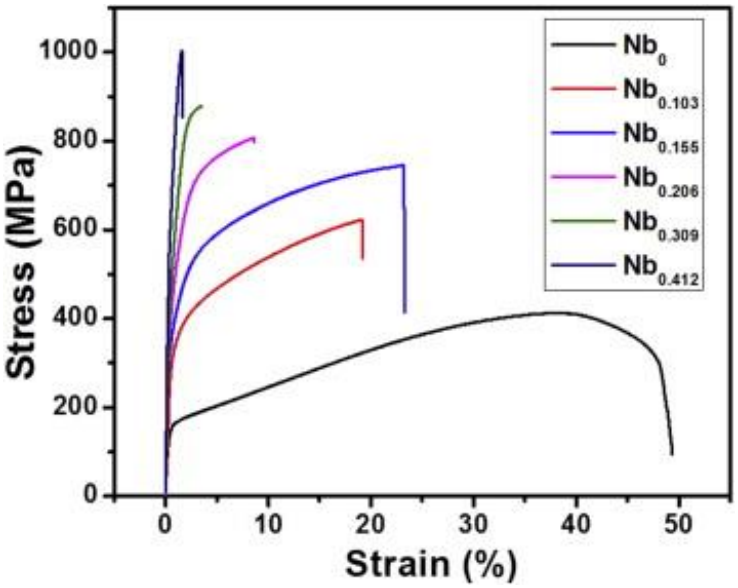

Figure 5: Stress-Strain Curves of CoCrFeNi-Nbx Alloys (Liu et al., 2015)

- Sluggish Diffusion

"Sluggish diffusion" has been a topic of debate within the community as researchers argue on what experimental methods and calculation techniques can provide accurate results of diffusion in HEA. It was believed that diffusion would be slower through a HEA versus that of a traditional alloy or pure metal. Interdiffusion in HEA was initially studied and classified as sluggish in studies performed by Tsai *et al.* (2013), the study involved the use of a pseudo-binary diffusion couple that mimicked many of the same principles used in the simple diffusion couple study. The study implied that if there was no shift of the Kirkendall interface it could be assumed there was no back diffusion and a modified Boltzmann-Matano method can be applied to calculate interdiffusion coefficients. The pseudo-binary diffusion couple relies on couples that vary two of the five HEA elements; couple specimens are welded together over a long period at elevated temperatures until a concentration gradient between the target elements is apparent, this concentration gradient can in turn be used to calculate interdiffusion coefficients.

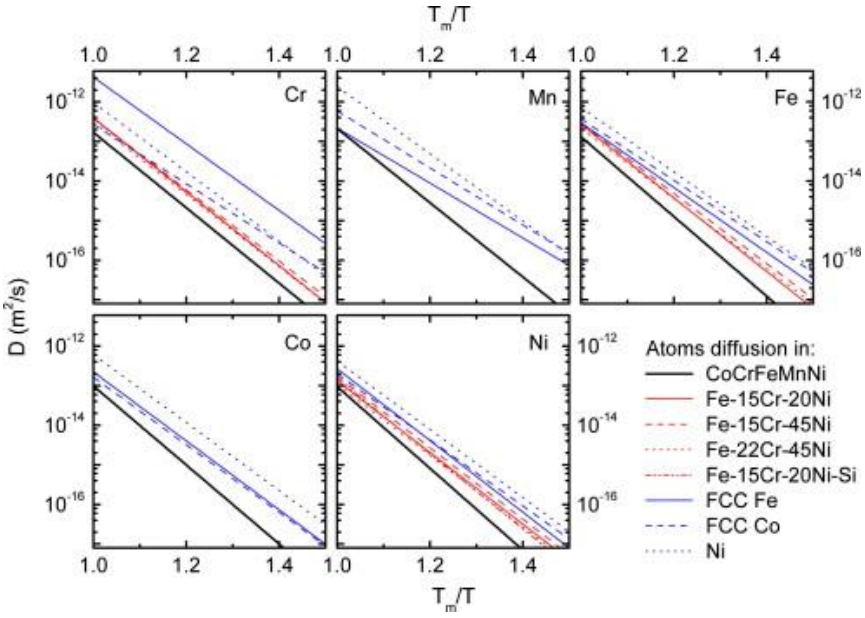

Figure 6: Arrhenius Plots for Diffusion Coefficients in a CoCrFeMnNi system from Tsai et al. (Tsai et al., 2013)

Tsai *et al.* compared Arrhenius plots between the Cantor HEA and multiple alloys (Tsai *et al.*, 2013) as shown in Fig. 6; the results concluded that the diffusion rate was slower in HEAs in every element tested in the Cantor HEA. Tsai postulated that because of the random scatter of elements in a matrix atomic potential traps may occur, where even though an atom may receive enough energy to move to the next vacancy in the matrix the new position may have a higher lattice potential energy (LPE) and thus the atom may move back to its original lower LPE location. Fig. 7 depicts how higher activation energy is required in HEA than that of a 3-component alloy and the disparity between the LPE values at each site.

Recent studies using the Calculation of Phase Diagrams (CALPHAD) approach and numerical simulations have agreed with Tsai's work it has been noted that this staggered diffusion witnessed is not inherently caused by the amount of key constituent elements. Kucza recorded lower diffusion coefficients in four-element HEA alloys versus what Tsai recorded in

the Cantor HEA (Kucza *et al.*, 2018). Following this, it seems that "sluggish diffusion" is not apparent in all HEAs (Divinski *et al.*, 2018), the consensus is that "sluggish diffusion" is not necessarily a core effect in HEA.

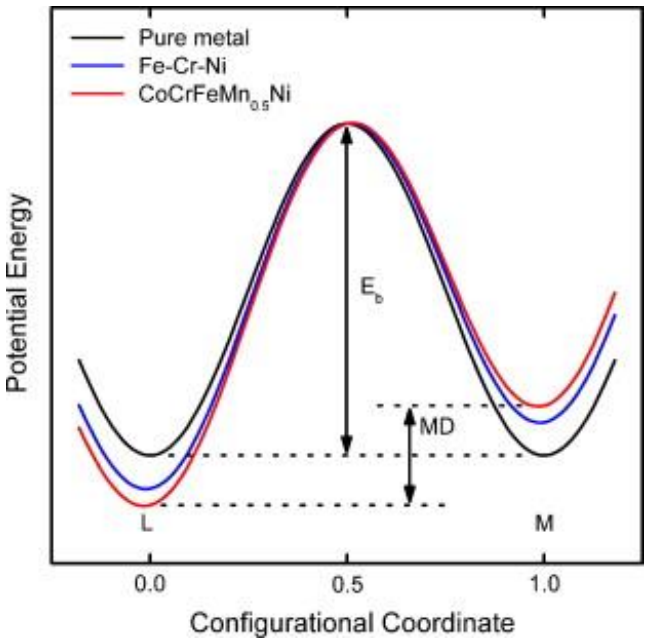

Figure 7: Lattice Potential Energy from Tsai et al. (Tsai et al., 2013)

1.3 Fabrication of HEA

- Conventional Fabrication of HEA

In most works related to producing HEA or compositionally complex alloys ingot metallurgy has proven fairly effective. Specifically, Arc melting has proven to be largely efficient in reaching the required temperatures to ensure full melting and mixing of multiple pure elements (Torralba et al., 2019). However, arc melting is limited to the production of simple structures and requires heavy machining to create parts of complex geometry.

Although HEAs have been produced through AM methods, including SLM (Hou *et al.*, 2021; Zhang *et al.*, 2019), to the best of the author's knowledge, no study has taken the proposed

LAA approach and instead rely on post-processing and or pre-fabricated or mechanically alloyed powders.

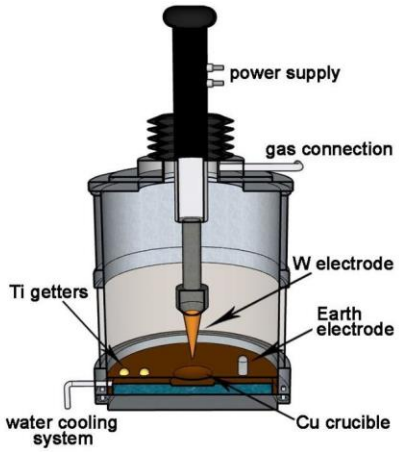

Figure 8 Schematic of Vacuum Arc Melting Chamber (Stansbury & Buchanan, 2000)

- Additive Manufacturing of HEA

Selective Laser Melting (SLM) is one type of additive manufacturing (AM) process that has drawn much attention. The SLM process involves powder distributed along a substrate which is subsequently selectively melted by a scanning laser. SLM can create complex near-net-shape products provided material powders and a STereoLithography (STL) file, Fig. 9 shows a simplified depiction of the SLM setup. It is important to note that there are many different AM methods and many that can be used to create HEA, such as Direct Energy Deposition (DED) or Spark Plasma Sintering (SPS), however, this paper will be limited to discussing the application of SLM.

The mixing process in the SLM melt pool is a rapid melting and freezing process that is largely driven by Marangoni force, and other properties, such as viscosity, density, and melting temperatures (Mosallanejad *et al.*, 2021). SLM method generally melts pure elemental powders

or prefabricated alloy powders. However, *in-situ* alloying of pure elemental powders during the SLM process allows for the freedom to create alloys with high degrees of customization and as such is a promising method for creating HEA, especially for fabricating the heterogeneous structures and changing material properties by adding additional elements in an HEA system. However, much is unknown about the diffusion process occurring in the melt pool and its effects on the formation of HEA as well as how this would ultimately affect the properties of the as-printed parts. Moreover, the empirical methods that have been used to calculate diffusion coefficients in HEA have been proven to be a source of controversy (Divinski *et al*., 2018; Kucza *et al*., 2018; Tsai *et al*., 2013). The LAA process involves the *in-situ* alloying of pure elemental powder when the powder bed is exposed to laser irradiation, this process requires that pure elemental powders are mixed to the prescribed compositions before the printing process begins (Hu & Li, 2017; Montiel *et al.*, 2019). The LAA process allows for the fabrication of specifically designed alloy parts, where prefabricated powders for high-performance materials may be difficult to source.

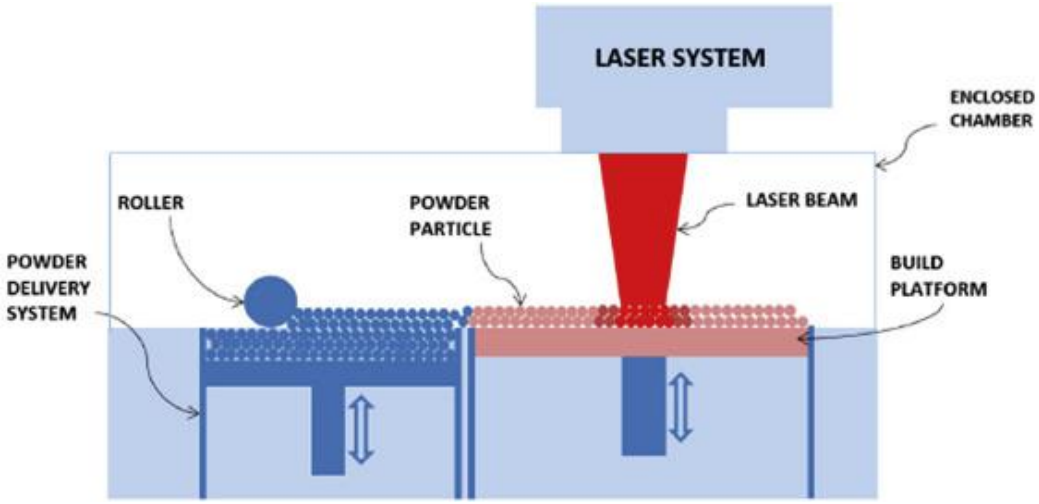

Figure 9 Demonstration of Selective Laser Melting Concept (Ahmed & Mian, 2019)

1.4 Knowledge Gap

Several studies have already been performed to create HEA parts in SLM (Hou *et al.*, 2021; Zhang *et al.*, 2019), however, most studies incorporate the use of prefabricated powders, mechanical alloying, or post-processing to create HEA. As far as the author is aware, no publication at the time this article is written has successfully produced a fully homogeneous HEA through the SLM method using pure elemental powders as proposed through the LAA method. Considering the complex nature of the LAA process, as well as the aforementioned possibility of "Sluggish" diffusion effects, the process of diffusion and mixing in the melt pool is a relative "black box" where only assumptions can be made. A better understanding of the diffusion and mixing in the melt pool during the LAA process is needed to postulate whether the diffusion occurring given the scale and rapid conditions is sufficient to facilitate the production of truly random HEA.

1.5 Research Questions and Hypothesis

Research questions proposed in this paper are as follows:

1.) What is the diffusion behavior is exhibited by pure multiple different elemental powders while induced to a rapid melting and quenching process like SLM? If pure elemental powders are rapidly melted and quenched, diffusion of elements in the melt pool will be severely limited and dependent on each powder's nearest neighbors.

2.) Does the increased entropy of a system affect the diffusion rate of its constituent elements in liquid form? If the configurational entropy of a system is increased, there will be no change of diffusion that can be directly linked to the entropy of the system.

Creating a better understanding of the diffusion in the melt pool in the LAA process can provide insight on what considerations must be taken to produce novel HEAs. The advent of the

LAA process and the understanding behind its mechanisms can allow for production of complex near-net shape parts made of compositionally complex alloys for industry.

In the next chapter, we will discuss the current methods used to measure diffusion coefficients in an experimental setting and the state-of-the-art works that attempt to quantify diffusion rate.

CHAPTER II

LITERATURE REVIEW

2.1 Diffusion and Diffusion Coefficients

To have a full understanding of diffusion it is important to understand the methods applied to quantify diffusion in both liquids and crystalline solids. This chapter is a literature review to discuss the calculation methods and experimental techniques used to quantify diffusion coefficients as well as describe the significance of such values. Diffusion in fluids was first quantified in 1855 by Adolf Fick with the identification of both of would be named Fick's Laws, these will be explained in the following sections.

2.1.1 Fick's Laws of Diffusion

Fick's First law can be described simply in isotropic media where both chemical and physical properties are independent of direction (Mehrer, 2007). The mathematical model can be described using a single-dimensional system, in this description particles can represent either atoms or entire molecules. Fick's first law in an isotropic medium is described below:

$$J_x = -D\left(\frac{\partial C}{\partial x}\right) \quad (1)$$

In Eq. (1), J_x represents the diffusion flux or the flux of particles in a single direction, C

is the concentration given at a location along a single direction. As diffusion flux is directly proportional to the derivative of the concentration gradient, D represents a factor of proportionality. D is referred to as the "Diffusion Coefficient", the units of the diffusion coefficient are given as length^2 per unit time (i.e. [cm^2s^{-1}], [m^2s^{-1}], or as referenced later in this paper [$Å^2ps^{-1}$]).

Fick's first law can also be described in vector notation to apply to a three-dimensional system, Fick's first law can be described as below:

$$J = -D\nabla C \tag{2}$$

where J represents the diffusion flux, D is the diffusion coefficient, and C represents the scalar concentration field C(x,y,z,t).

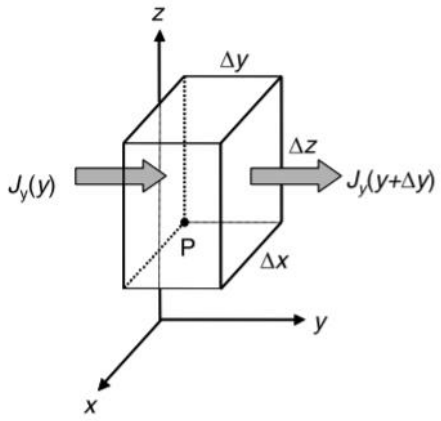

Figure 10: infinitesimal control volume, where Jy represents the flux moving in the Y direction (Mehrer, 2007)

Fick's Second law, known as the "Diffusion Equation", is a combination of Fick's first law equation and the equation of continuity; the diffusion equation is given as follows:

$$\frac{\partial C}{\partial t} = \nabla * (\mathrm{D}\nabla \mathrm{C}) \tag{3}$$

At first glance Fick's second law is a second-order differential equation; wherein if the diffusion coefficient, D, is dependent on the concentration the equation becomes non-linear, this is the case in what is commonly known as Interdiffusion and will be covered in section 2.1.2. In the case that the diffusion coefficient is not dependent on local concentrations the system is more indicative of self-diffusion or tracer diffusion, where the previous equation can be simplified as:

$$\frac{\partial C}{\partial t} = D\Delta C \tag{4}$$

where Δ is the Laplace operator and C is a function C(x,y,z,t), solutions to this model will be discussed in section 2.1.3.

2.1.2 Interdiffusion

Assuming diffusion in a single direction, i.e., the diffusion couple example, Fick's second law can be simplified to the following:

$$\frac{\partial C}{\partial t} = \frac{\partial}{\partial x}\left[D(C)\frac{\partial C}{\partial x}\right] = D(C)\frac{\partial^2 C}{\partial x^2} + \frac{dD(C)}{dC}\left(\frac{dC}{dx}\right)^2 \tag{5}$$

Ludwig Boltzmann introduced a new variable to the system to transform the equation to a nonlinear ordinary differential equation in 1894 (Boltzmann, 1894) shown below:

$$n \equiv \frac{x - x_M}{2\sqrt{t}} \tag{6}$$

Applying the new variable to equation (5) the system can be simplified as shown below:

$$-2n\frac{dC}{dn} = \frac{d}{dn}\left[D(C)\frac{dC}{dn}\right] \tag{7}$$

This transformation allows for the calculation of the interdiffusion coefficient via the Boltzmann-Matano method. There are several limits to this model:

1. The Boltzmann-Matano equation assumes a semi-infinite system, this would mean when considering a diffusion couple this equation is not applicable if the left and right boundaries of the diffusion couple are corrupted by the diffusion process.
2. Near the left and right boundaries of the diffusion couples, there can be a significant error because the differential of the concentration curve becomes very small.
3. When using the diffusion couple method with alloys, it is important to note that diffusion from specimen A is not inherently equal to diffusion from specimen B. This results in the Kirkendall effect, the Boltzmann-Matano method is not appropriate in this situation.
4. This equation also assumes constant volume throughout the entire diffusion process.
5. The Matano plane must be located to use this solution.

Sauer-Freise (Sauer & Freise, 1962) developed two follow-up equations that can be used to calculate the diffusion coefficients without finding the Matano plane as well as to account for Volume change as a result of the diffusion process.

Experimentally diffusion couples are formed through welding 2 or more specimen (Chen & Zhang, 2017; Dayananda & Sohn, 1999.; Li *et al*., 2016) together and allowing ample time at elevated temperatures to create a concentration gradient of the elements of focus, to measure the gradient methods such as mechanical sectioning, EPMA, and EDS (Tsai *et al.*, 2013) with standards are appropriate. This in turn allows calculation via means of Boltzmann-Matano, Sauer-Freise, or Darken methods.

2.1.3 Tracer and Self Diffusion

When the diffusion coefficient is not dependent on concentration and only dependent on time and pressure, the coefficient is generally referred to as a tracer or self-diffusion coefficient. This term applies to any system that is not dependent on concentration, thus applicable to atoms in a pure element as well as elements of interest in a sufficiently homogenous alloy. Experiments involving this calculation typically use a thin film applied to a material in either a topical application, as in simply on one side of a bulk specimen, or in a "sandwich" where the thin film is applied between two bulk specimens. Usually, a radioactive isotope is chosen as "tracers" that can be detected later on to define the concentration gradient. The simplified solution to the thin film experiment is denoted below:

$$C(x,t) = \frac{M}{\sqrt{\pi D t}} \exp\left(-\frac{x^2}{4Dt}\right) \tag{8}$$

where M denotes the number of atoms or particles diffusion per unit area, D is the tracer diffusion coefficient, t is time, and x is the distance into the bulk specimen referenced from the initial thin film. It should be noted that when the experiment is prepared as a "sandwich" the right side of the equation is to be divided by 2 (Mehrer, 2007).

2.1.4 Molecular Dynamics Study of Diffusion Coefficients

Molecular Dynamics (MD) provides a unique numerical framework to measure the atomic transport in the powder bed, since studying the rapid melting and cooling SLM process experimentally could be an arduous task. However, atomistic studies performed on MD software have been able to mimic AM methods such as selective laser sintering (SLS) (Butrymowicz *et al.*, 1973; Lewis *et al*., 1997; Nandy *et al*., 2019; Raut *et al*., 1998; Song & Wen, 2010; Wakai, 2006; Yang *et al.*, 2012) and SLM (Chen *et al.*, 2020). MD can be used to predict the formation,

segregation, and mobility in a crystal lattice *(Chen et al., 2020; Ding et al., 2018b; Jiang et al.*, 2020). Inspired by these works, MD simulation can be applied to explore the mobility of atoms in the Cantor HEA powder bed, the behavior occurring in both the rapidly melting and freezing melt pool, the effects of laser parameters on the formation of HEA, and the feasibility of its production in the SLM process can be studied. Classical MD initially requires the input of atom to atom potentials and the initial position and velocities for each atom. Based on the given potentials, interatomic forces can be calculated as well as the resulting motion. After which the simulations can calculate the systems energy, temperature, and pressure, amongst other parameters of interest. After a time step, the necessary data is stored and used as the initial information to repeat this calculation for the next time step. Fig. 11 lays out this process in a simple format.

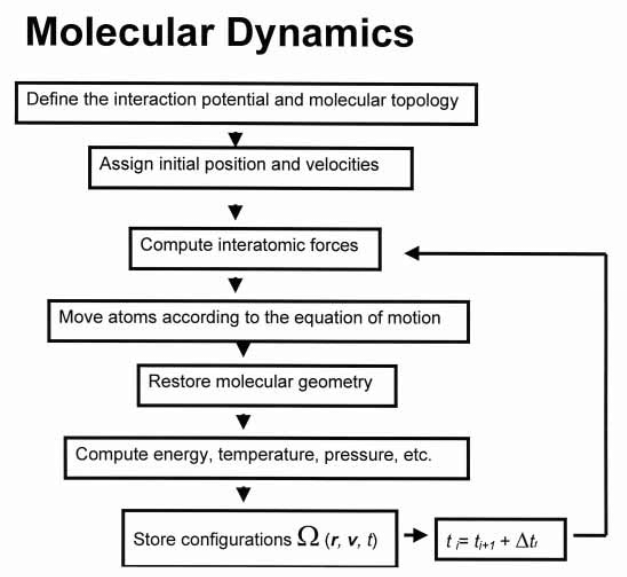

Figure 11 Molecular Dynamics Breakdown (Grigera, 2005)

For a metallic system, Embedded Atom Method (EAM) is a popular semiempirical method that has proven well suited for FCC crystal structures. Modified Embedded Atom

Method (MEAM) follows a similar model but includes angle-dependent terms allowing for directional bonding to be considered. Energy in either EAM and MEAM systems can be modeled by:

$$E = \sum_i \{F_i(\overline{\rho_i}) + \frac{1}{2}\sum_{i \neq j} \emptyset_{ij}(r_{ij}) \quad (9)$$

Where r_{ij} is the distance between a given body and its neighbor, $\emptyset_{ij}$ is a pair potential function between atom pairs, and F is embedding energy that is a function of ρ or electron density (Daw & Baskes, 1983).

For MEAM potential the embedding energy $F_i(\rho_i)$ can be expressed as:

$$F_i(\overline{\rho_i}) = A_i E_i^0 \overline{\rho_i} \ln(\overline{\rho_i}) \quad (10)$$

where A_i is an adjustable parameter, and E_i^0 is the cohesive energy of an atom *i* in a reference structure. As far as this study is confirmed, the MEAM potential is considered the most appropriate to calculate the interactions in HEA.

In this study, we will perform an MD simulation to explore the diffusion behavior on a random powder bed, as well as the effects the rapid process has on the material of the as-printed product. Further studies were used to explore the tracer diffusion behavior of an equilibrium system as it is related directly to the entropy and complexity of the systems. In the next chapter, the MD simulation setup, considerations, computational resources are discussed in detail

CHAPTER III

METHODOLOGY

All MD simulations were performed using the Large-scale Atomic/Molecular Massively Parallel Simulator (LAMMPS) open-source software (*LAMMPS Molecular Dynamics Simulator*, n.d.; Plimpton, 1995) and visualized using OVITO (Stukowski, 2010). The studies involved in this thesis are organized in several parts to target specific areas of interest as enumerated below:

1. Powder Bed Studies: these studies are intended to directly observe the diffusion processes in the rapid freezing and melting of the powder bed, this study is also needed to create "samples" for the second proposed study.
2. Property Studies: these studies rely on "samples" exported from the previous studies. These samples are used to simulate material properties to give some understanding of what effects the AM fabrication method can result in.
3. Diffusion and Entropy: This is a separate study studying equilibrium methods to determine the self-diffusion of elements in various alloys. This study is intended to observe what effects entropy and alloy composition have on the diffusion coefficients of its constituent elements.

3.1 Methodology and Simulation Setup of the Powder Bed

The study incorporated 121,524 atoms: 104,196 Fe atoms (including both substrate and

powder atoms), 3860 Cr atoms, 4576 Ni atoms, 4468 Co atoms, and 4424 Mn atoms. The simulation domain can be found in Fig. 12, where the domain was designed specifically to avoid any adjacent duplicate elemental powders, and the powders were also situated far from the x and y boundaries to isolate the simulation. The MEAM potential was chosen from the NIST repository as a result of studies by Choi *et al*. (Choi et al., 2018). To simplify the model, all powder diameters were chosen to be the same, due to varying lattice parameters, atoms per powder vary with each element. All powders and substrate powder were created using Atomsk (Hirel, 2015); Mn powder, due to its complex α-phase structure (Hobbs et al., 2003), was constructed as a simple BCC crystal structure and melted at 2000K and cooled to room temperature, 300K, over 1000 ps until structure reached an equilibrium. The stabilized structure was replicated and cut into a spherical powder for use in the MD study. Besides the Mn powder, the lattice parameters for other elemental powders used in the MD simulation can be found in Table1.

Table 1 Crystal Lattice Parameters for Fe, Co, Cr, Ni

Element	Crystal type	Lattice Parameter
Fe	BCC	*a = 2.871*
Co	HCP	*a = 2.507, c = 4.507*
Cr	BCC	*a = 2.91*
Ni	FCC	*a = 3.52*

The powder bed system was modeled with periodic boundary conditions in the x and y direction and a shrink-wrap boundary condition in the z-direction. Initially, the system was equilibrated at 300K using an NVT ensemble for 10 ps, after which the powder bed was equilibrated at 300K using a Langevin thermostat and an NVE fix for 10 ps. After which the substrate's temperature was controlled by a Langevin thermostat to maintain a temperature of

300K and serve as a vector of heat transfer out of the system, cooling the powder bed. A laser scan was simulated starting at x = 80 Å and y = 143.11 Å and swept down a path in the x-direction. The laser was simulated using a heating power of 400 eV/ps over 3 different scanning velocities to determine the effect of energy density on the powder bed, and the parameters can be found in Table 2. Evaporated atoms expand the simulation cell indefinitely and thus significantly raise computational requirements; to remedy this, an evaporation fix is set above the powders. The Evaporation fix removes any atoms that raise above the coordinates Z > 43Å and allows for the shrink-wrapped Z boundary to remain minimal.

Table 2 Laser Parameters for Single Track Study

Test No.	Power (eV/ps)	Velocity (nm/ps)	Energy Density (J/mm^3)
1	400	0.060	46.54
2	400	0.045	62.06
3	400	0.030	93.08

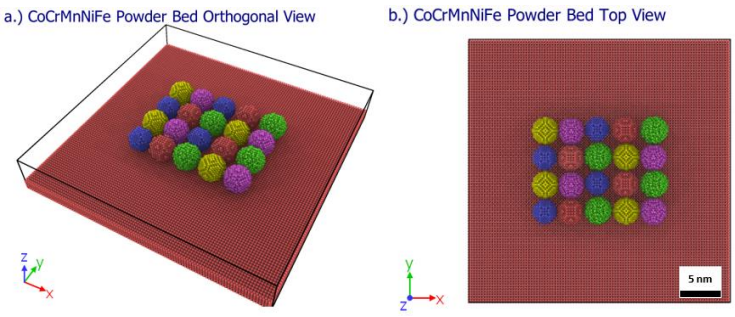

Figure 12 (a) isometric preview of powder bed model used in MD study (b) top-down perspective of powder bed model, red circle indicates approximate dimensions and start location of the laser. Powders are colored accordingly: green is Mn, yellow is Ni, blue is Cr,

A follow-up study with two laser tracks was studied incorporating a meander hatch strategy. The laser strategy used 0.03 nm/ps scan speed and a 6 nm hatch distance, this can be seen

in section 4.2.

3.2 Methodology and Simulation Setup for Young's Modulus and Lattice Thermal Conductivity

For this study, three major properties were chosen as a focus, namely Young's Modulus, Shear Modulus, and thermal lattice conductivity. These material properties were chosen to determine the validity of additively manufactured high entropy alloys in general applications, as well as the possibility of using these materials in renewable energy applications.

- Conductivity coefficients

There is an important distinction that must be made about the thermal conductivity values gathered as a result of this study; total thermal conductivity coefficient is considered a sum of two components, the lattice thermal conductivity coefficient, and the electric conductivity coefficient, and can be modeled by the equation below, where k_l is the lattice contribution and k_e is the contribution from free-electron interactions:

$$k_{total} = k_l + k_e \tag{10}$$

Classical MD studies are limited in that they cannot model the heat transfer that results from free-electron interactions, this mode of heat transfer is dominant in most crystalline structures. Due to this limitation, this study is limited to calculating the lattice thermal conductivity through means of MD, any calculation of total conductivity coefficients is purely inferred based on known electrical resistivity constants, Lorenz factor, and the Wiedemann-Franz-Lorenz (WFL) relation.

To calculate lattice thermal conductivity the Green-Kubo formalism was adopted; this model is an Equilibrium Molecular Dynamics (EMD) method that allows for smaller simulation

cells while allowing for samples to be taken from near-cube-like dimensions. Green-Kubo method involves a system held at equilibrium at 300 K; The heat flux is then calculated in a J tensor, which can be seen below:

$$\boldsymbol{J} = \frac{1}{V}\left[\sum_i e_i \boldsymbol{v}_i - \sum_i \boldsymbol{S}_i \boldsymbol{v}_i\right]$$

$$= \frac{1}{V}\left[\sum_i e_i \boldsymbol{v}_i + \sum_{i<j}\left(\boldsymbol{f}_{ij} \cdot \boldsymbol{v}_j\right)\boldsymbol{x}_{ij}\right]$$

$$= \frac{1}{V}\left[\sum_i e_i \boldsymbol{v}_i + \sum_{i<j}\left(\boldsymbol{f}_{ij} \cdot (\boldsymbol{v}_i + \boldsymbol{v}_j)\right)\boldsymbol{x}_{ij}\right] \quad (11)$$

where V is the volume of the system, e_i is the per-atom energy, v_i is the per atom velocity, S_i is the per-atom stress tensor, and f_{ij} is the force between two atomic bodies. An autocorrelation is then performed and the result is then integrated with respect to time using a trapezoidal method as shown below:

$$k = \frac{V}{k_B T^2}\int_0^\infty \langle J_x(0) J_x(t)\rangle \, dt = \frac{V}{3k_B T^2}\int_0^\infty \langle J(0) \cdot J(t)\rangle \, dt \quad (12)$$

where k_B is the Boltzmann's constant and T is the Temperature of the system.

In this study, an initial model of completely random solid CoCrMnNiFe was studied using the Green-Kubo method to verify that the model is capable of reliably calculating lattice thermal conductivity coefficient, after which the model was then used to test the lattice thermal conductivity of the powder bed results from the study explained in section 3.1.1. Initially, the model is equilibrated using a constant volume and temperature NVT ensemble at 300 K for 10,000 time steps; for this model, a single timestep is considered 0.001 picoseconds. After the equilibration period, the model has an NVE ensemble imposed, this ensemble does not employ a thermostat and prevents the system from losing or gaining energy while still allowing for kinetic behavior in the simulation cell, for 500,000 timesteps until a final conductivity coefficient can be

calculated. Initially, a random solid solution was studied to verify the model. Furthermore, a study was conducted on the results from the previous powder bed simulation to determine what effects SLM would have on the lattice thermal conductivity.

- Young's and Shear Modulus

Metallic single crystals can exhibit anisotropic behavior, as such a small lattice structure can exhibit 36 elastic constant values as shown in the general relation between stress, strain, and elastic constants:

$$\begin{bmatrix} \sigma_1 \\ \vdots \\ \sigma_6 \end{bmatrix} = \begin{bmatrix} C_{11} & \cdots & C_{16} \\ \vdots & \ddots & \vdots \\ C_{61} & \cdots & C_{66} \end{bmatrix} \begin{bmatrix} \varepsilon_1 \\ \vdots \\ \varepsilon_3 \end{bmatrix} \tag{13}$$

Metals generally are symmetric in the X, Y, and Z axes assuming the system is cubic, therefore, C_{11}, C_{12}, C_{44} are unique, as all other components of the elastic tensor are typically equal to zero. Thus the Voigt averaging method can be used as listed below:

$$B = \frac{C_{11}+2C_{12}}{3} \tag{14}$$

$$G = \frac{C_{11}-C_{12}+3C_{44}}{5} \tag{15}$$

$$E = \frac{9GB}{3B+G} \tag{16}$$

where B is the Bulk Modulus, G is the Shear Modulus, and E is Young's Modulus (Shinoda *et al*., 2007).

Initially, like the conductivity model, the model was tested using a random solid solution Cantor alloy monocrystal composed of 4000 atoms to verify if the calculation. The Young's and shear modulus were acquired from the powder bed created as a result of the two-track laser study discussed in section 3.1.1, a section was cut from the powder bed and used to calculate material properties considered the nonhomogeneous distribution post melting.

3.3 Simulation of Diffusion Coefficients

The following section describes how simulations were set up to study diffusion coefficients in multiple equilibrium systems. Although several simulations were performed for comparison, the MD script is nearly identical in both situations. All studies were performed using a cubic simulation cell encompassing a crystal lattice with 32000 atoms to allow for adequate averaging. All systems followed the same steps:

1. Equilibrated at 300 K using an isobaric NPT ensemble at 1 bar for 100,000 timesteps.
2. The temperature of the system is gradually raised to 3000 K using an isobaric NPT ensemble at 1 bar for 100,000 timesteps.
3. Equilibrate at 3,000 K using an isobaric NPT ensemble at 1 bar for 200,000 timesteps
4. Gradually lowering the temperature of the system to 1,607 K, the liquidus temperature of the cantor alloy, with an isobaric NPT ensemble over 1,000,000 timesteps.
5. Equilibrate at 1607 K using an isobaric NPT ensemble at 1 bar for 200,00 timesteps.
6. Reset time step count.
7. Run system with NVT ensemble at 1607 K while calculating the Mean Squared Displacement (MSD).

MSD can be calculated using the equation listed below:

$$MSD = \langle r^2(t) \rangle = \langle \frac{1}{N} \sum_{i=0}^{N} \big(r_i(t) - r_i(0) \big)^2 \rangle \quad (11)$$

where $r_i(t) - r_i(0)$ is a vector distance traveled by a particle, N is the number of particles, and t is time. The time derivative of the MSD is proportional to the tracer diffusion coefficient as shown below (Pranami & Lamm, 2015):

$$D = \frac{1}{6}\frac{d}{dt}(MSD) \quad (12)$$

This calculation takes longer wall times to ensure that the diffusion coefficient value converges, hence the 800,000 timesteps required in step 7.

As mentioned before, The diffusion study took two different approaches to study the effects of system configurational entropy on tracer diffusion coefficients, the first study focused on comparing the diffusion rates in the cantor alloy and more simple solute-solvent alloys; while the second study compared equimolar systems with fewer components. The two will be discussed in more detail below:

- Comparison of Diffusion Rates between Cantor alloy and Solute-Solvent based alloys

In this study, configurational entropy of the system and diffusion coefficients were compared directly, configurational entropy in this study was varied by increasing the Fe content in the system by 20% intervals while maintaining the remainder 4 elements at equimolar proportions to each other, for example, the final test involved a system with 80% Fe-5%Co-%5Cr-5%Ni-5%Mn. the overall entropy of the alloy systems was calculated using the following equation:

$$\Delta S_{conf} = -R * \sum_{i=1}^{n} x_i ln x_i \quad (13)$$

- Comparison of Diffusion Rates between Cantor alloy and other Equimolar Systems

In this study, the diffusion coefficients of 3 equimolar alloy systems were compared: CrNiFe, CoCrMnNi, and CoCrMnNiFe. Systems with fewer components, in effect, have lower configurational entropies, and as such, this is an indirect relationship between configurational entropy and diffusion. These alloys were chosen due to the abundance of published information

on their properties and diffusion behavior.

3.4 Computational Resources and Acknowledgment

This work used the Extreme Science and Engineering Discovery Environment (XSEDE), which is supported by the National Science Foundation grant number ACI-1548562. This work used XSEDE Stampede2 at TACC through allocation TG-CTS200013 and Bridges2 at PSC through allocation TG-MCH200010. For studies mentioned almost all studies were run on a single node with 96 cores for optimal efficiency. These studies were also supported using the UTRGV HPC cluster, THUMPER.

CHAPTER IV

RESULTS AND DISCUSSION

4.1 Single-track Studies

In this section, two sets of MD simulations were performed to explore the effects of diffusion of elements in HEA systems when two different laser scanning strategies were adopted. This section, 4.1, will discuss the results from the single-track study in particular.

4.1.1 Study of laser energy density and diffusion

Fig. 13 depicts the top view of the melt pool as the laser irradiates powders over time from *t=0 ps* to *t=200 ps*. Mn was more unstable than its counterparts and as a result, broke apart much quicker as the heat transferred to their lattices.

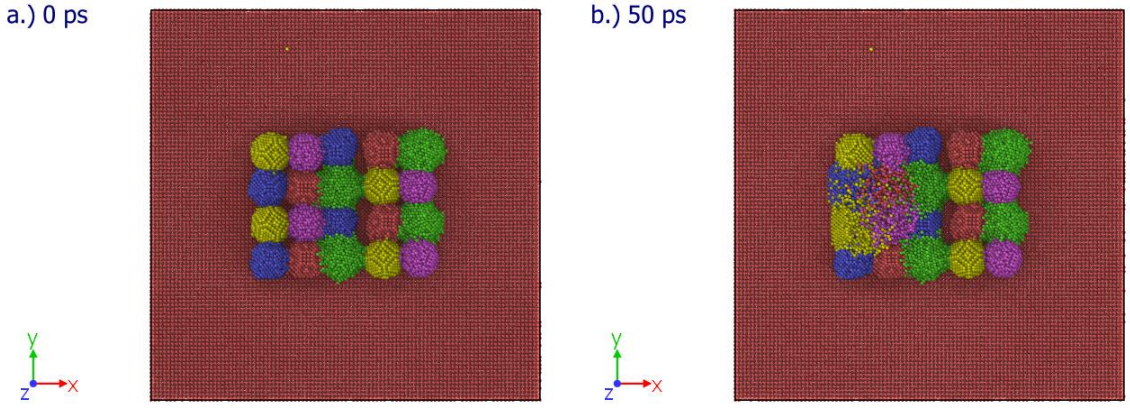

Figure 13 Time series of powder bed with a 0.06 nm/ps laser scan speed over 200 ps

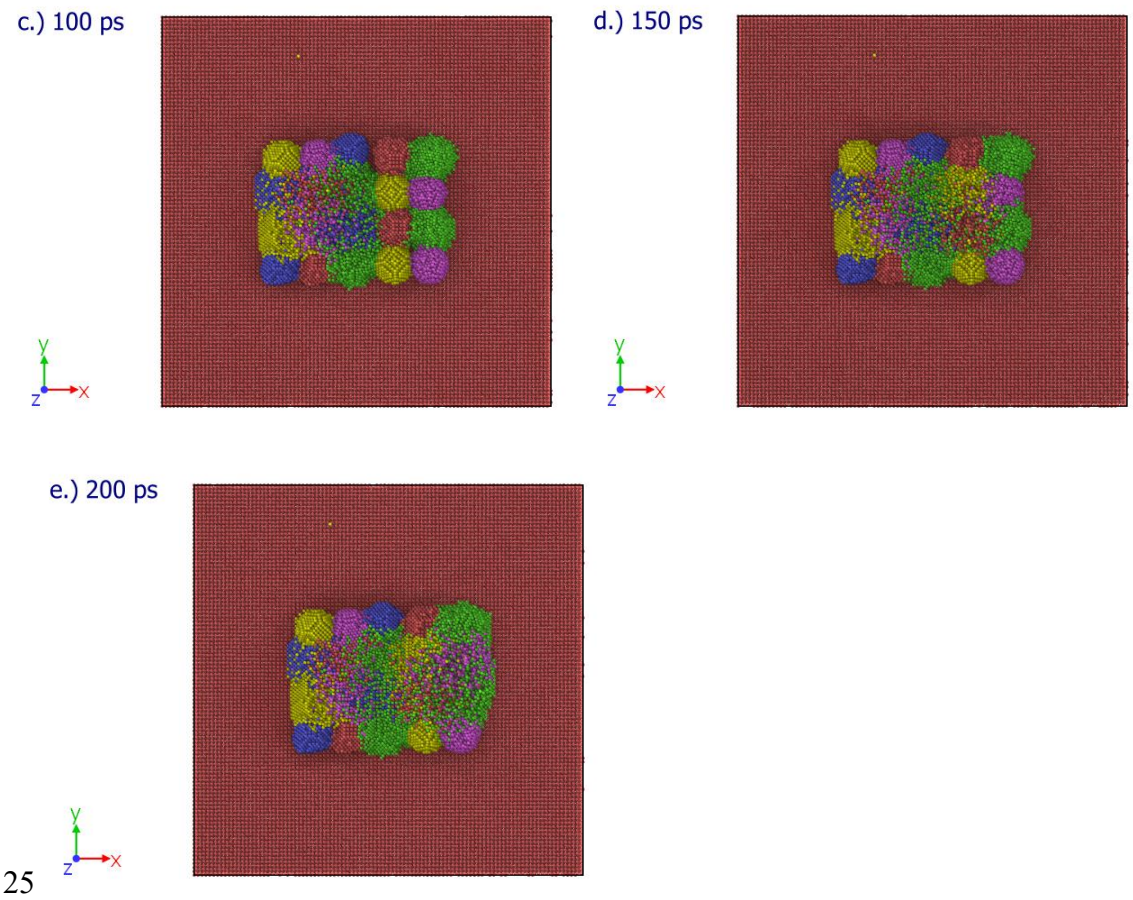

25

Figure 143 (continued)

Diffusion in a powder bed system is a complicated process that differs much from the ideal parameters presented in empirical approaches such as the diffusion couple or self-diffusion studies (Song & Wen, 2010). Early powder bed diffusion is driven largely by surface contact with neighboring particles (Wakai, 2006). A major advantage of using the MD approach is the ability to observe diffusion behavior per atom instead of through empirical methods. In this study, the MSD approach was used to study the transport of selected atoms in Fig. 3, the MSD calculation can be seen in Eq. 11 in Section 3.3. MSD can be compared among different elements with respect to their original powder cluster to gain an understanding of the occurred average displacement.

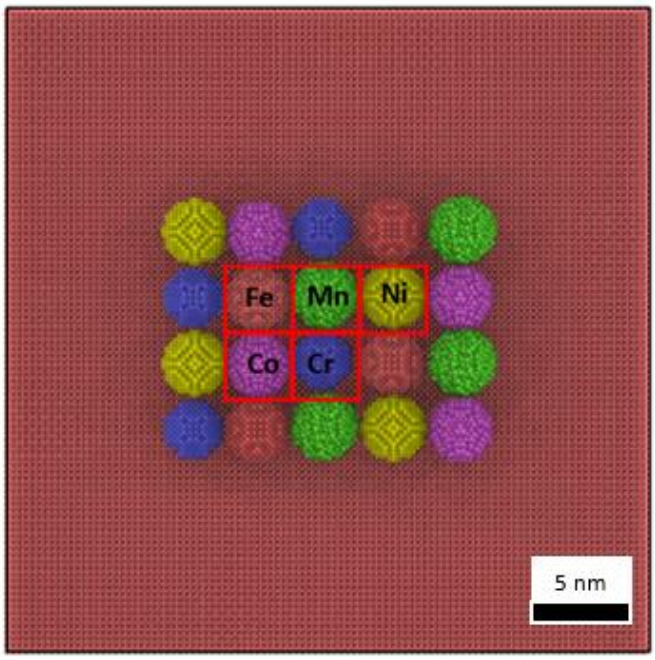

Figure 14 Powders selected for study, atoms in these regions were also studied independently

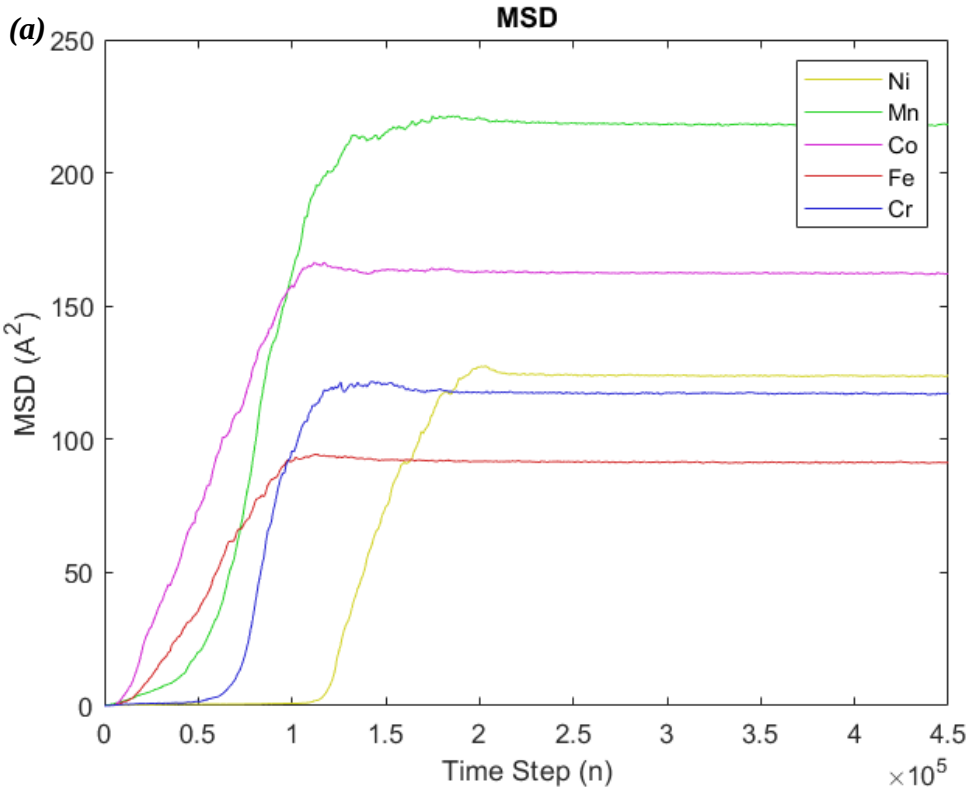

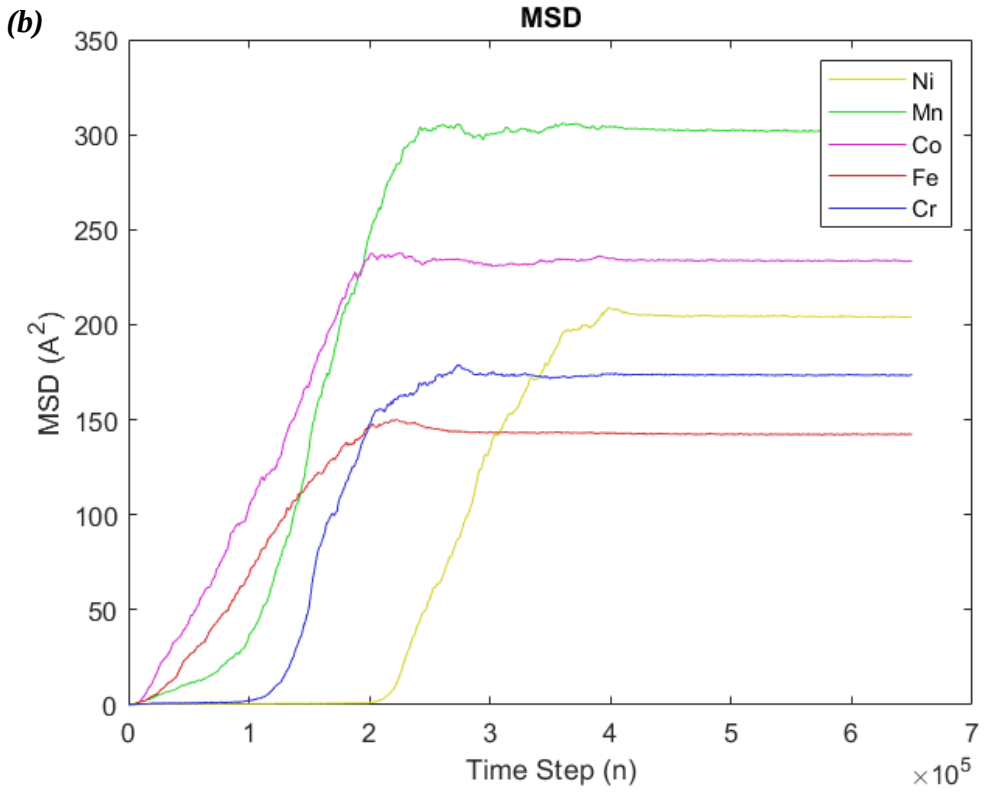

Figure 15 Mean Square Displacements of atoms selected a group based on what particle it was a constituent under a laser with scanning speed (a) 0.060 nm/ps and (b) 0.030 nm/ps.

MSD results were expected to exhibit non-linear mobility in the early melting process, initially, atoms dissociate from their local lattice and move freely to fill voids in the powder bed. In the mesoscale, the different elements upon contact would experience composition driven diffusion; however, as the laser leaves a region the diffusion of the elements in the area eventually becomes minuscule as the system freezes and crystallizes, this is indicated as the MSD curve plateaus and trends towards a constant value. As shown in Fig. 15, the MSD plateaus trended different constants based on the three different scanning speeds, and both Mn and Co exhibited significantly higher MSD than the other elements of the system. In addition, slower laser scanning speed resulted in higher MSD values, which also indicated that slow scanning speed could provide more energy to local particles and promote melting and diffusion, but there is some risk of burnout

if the laser is moving too slowly.

Atomic diffusion is largely affected by the energy incident on any given atom. Moreover, the initial environment of a given atom can have a large effect on the ability of an atom to diffuse (Zener, 1951). Given the initial configuration of the powder bed, the MSD of the given elements would suggest that Cr, Fe, and Ni have some difficulty in diffusing during the alloying and melting process. However, in studies by Hou *et al.* (2021) it was noted that Cr has difficulty in fully melting at varying energy densities in additively manufactured FeCrCoNi alloy. This may suggest that special care should be considered when selecting these powders; for example, choosing smaller powder diameters for the given elements could help promote melting and diffusion. Based on the linear portion of each MSD curve in Fig. 15b, the diffusion coefficient was calculated to roughly characterize the atomic diffusion, as shown in Table 3.

Table 3 Average Diffusion Coefficient

D ($Å^2$/ps)	Co	Cr	Fe	Mn	Ni
This Study	0.212	0.326	0.146	0.374	0.240
Ding *et al.* (2018)	0.182	0.196	0.183	0.193	0.181

It is worth noting that these values were not constant and only represented the behavior in this situation. However, this is qualitatively aligned with results from studies with Yeh *et al.* (2013) and Ding *et al.* (2018), therefore our MD model can be verified in a reasonable range. Although it is expected that there must be a similar degree of diffusion from all constituent atoms in a system to promote homogeneity in a final product, accelerated diffusion of an element can also indicate rapid segregation, but there was no apparent observable segregation in this study.

4.1.2 Energy density and composition in single track study

Images of individual atoms were taken for each constituent element in the system, they were then reduced to a binary image and overlayed in an in-house MATLAB program (*MATLAB*, 2019) to provide a qualitative analysis of diffusion throughout the powder bed by investigating the mixing of various pixels. The in-house MATLAB program can count how many different elements are existent on any single given pixel; assigning each pixel a value between 0 and 1, where 0 indicates the presence of no elements, 0.2 indicates the presence of 1 element, 0.4 the presence of 2 elements, etc. up to the maximum value of 1 which indicates the existence of 5 elements on a given pixel. According to this analysis strategy, Fig. 16 shows the pixel overlay analysis for the melt powder bed under different laser scanning speeds, and this is intended to provide a topical analysis of the location where the high entropy alloy may be formed. As expected, as the laser scanning speed was lowered, there was a significant increase in pixels with 4 or 5 elements present, and the percentage of 4 and 5 element pixels in the 0.03 nm/ps laser then doubled the percentage present in the simulation using 0.06 nm/ps.

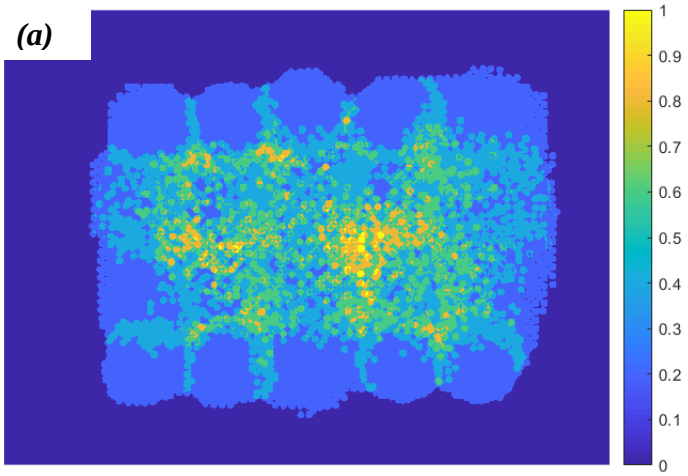

Figure 16 Pixel overlays of the powder bed under three different scanning speeds (a) 0.060

nm/ps; (b) 0.045 nm/ps, and (c) 0.030 nm/ps, respectively.

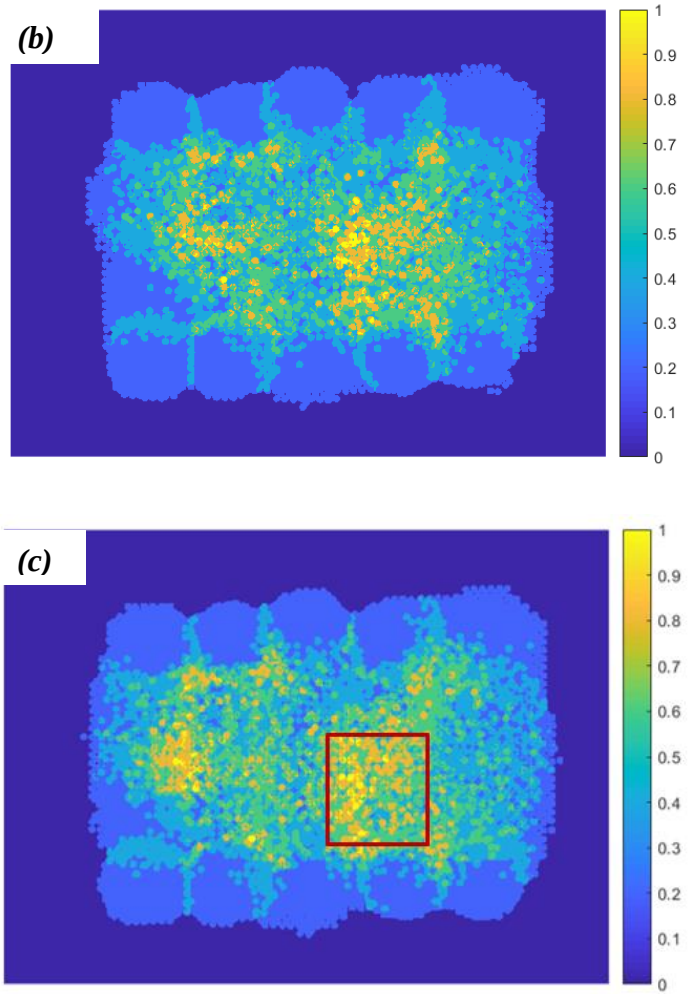

Figure 16 (Continued)

As shown in Fig. 16c, the indicated area shows the best pixel mixing, therefore there was a high chance that HEA would be formed. To further analyze the material composition in the boxed area in Fig. 16c, Fig. 17 shows the atomic percentage of each element. The area was expected to have a strong presence of all 4 elements, and Fe appeared in a much larger percentage as this was the original site of a Fe powder at the start of the simulation, whereas Cr was only found minimally in the location despite a Cr powder being directly adjacent to this location in the original powder configuration, as shown in Fig. 14. As noted in Figs. 14a and 14b, Cr and Fe exhibited the lowest

MSD through the process, this may be an indication that both elemental powders may only melt for only a short amount of time before re-solidifying.

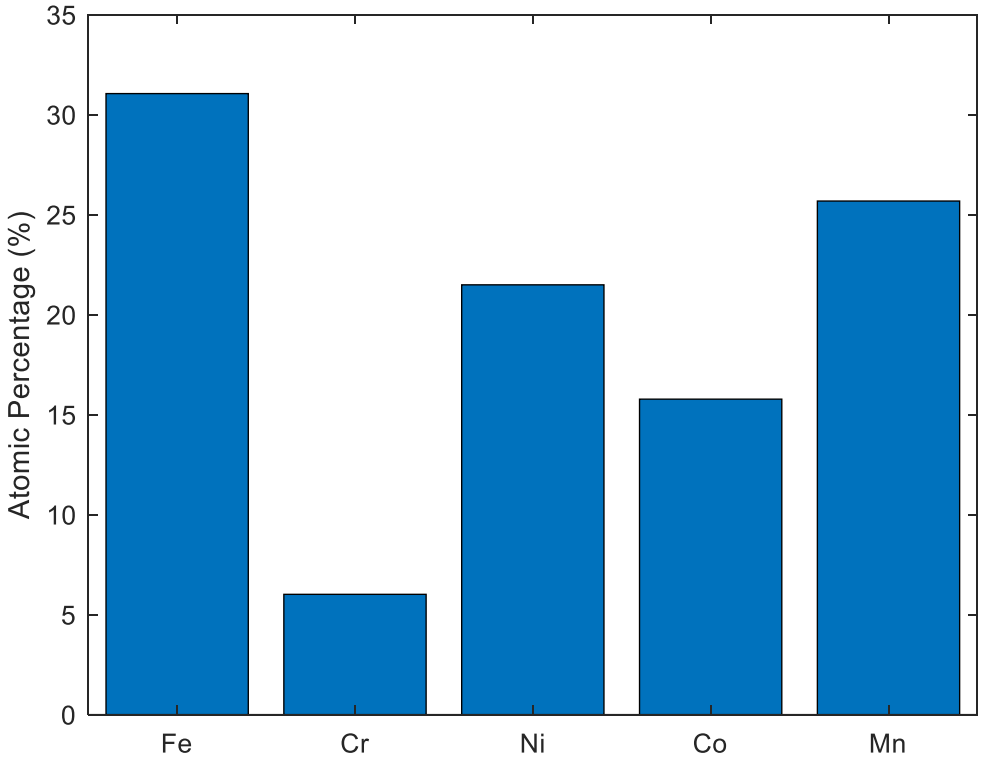

Figure 17 Composition of the area indicated in Fig. 15c

4.1.3 Crystal Structure of Single-Track Studies

PTM analysis was performed on the equilibrated, room temperature powder bed. In Fig. 18, there was no clear change in the crystallization of the powder bed with varying scan speed; in each hatch, HCP crystal was dominant with some distributed FCC crystal structure. The majority of the remaining BCC crystal structure appears to exist in the unmelted BCC particles in the powder bed. While the majority of the FCC-HCP structures appear through the path of the laser; some BCC structure lies on this path as well and it would appear that this may be a result of BCC elements Fe and Cr are only briefly activated to diffuse and as such didn't allow for much

movement from their local structures.

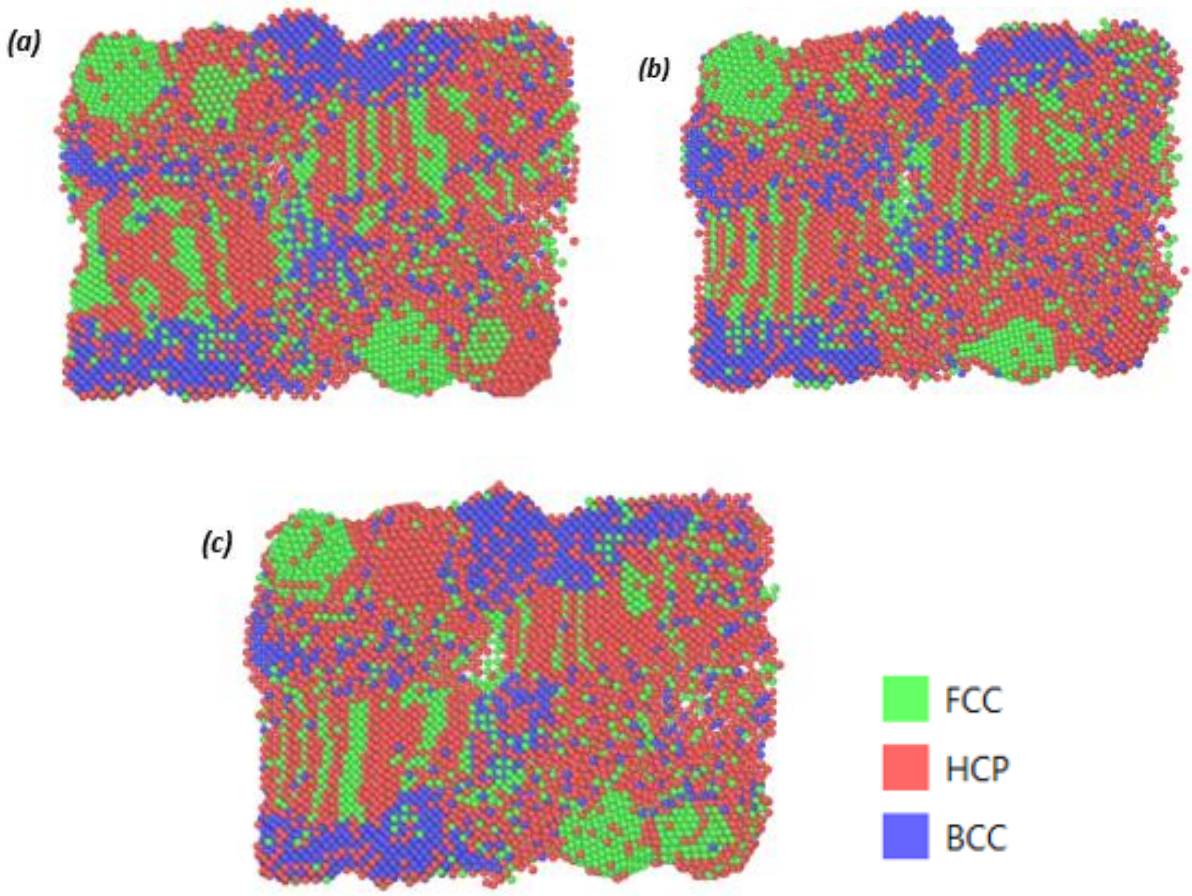

Figure 18 Polyhedral Template Matching (PTM) Analysis of solidified powder bed after (a) 0.06 nm/ps (b) 0.045 nm/ps, (c) 0.03 nm/ps scanning speeds

4.2 Multiple laser track study

4.2.1 Multiple Track Study and diffusion

Considering the best case from the single-track studies, a follow-up study was performed with 2 laser tracks operating in a meander pattern using the 0.030 nm/ps scan speed with a hatch distance of 6 nm. The laser started from the upper left of the powder bed and returned from the lower right of the powder bed. There is only one present laser in the simulation at any given time,

and Fig. 19 displays the laser diameter and its scanning path.

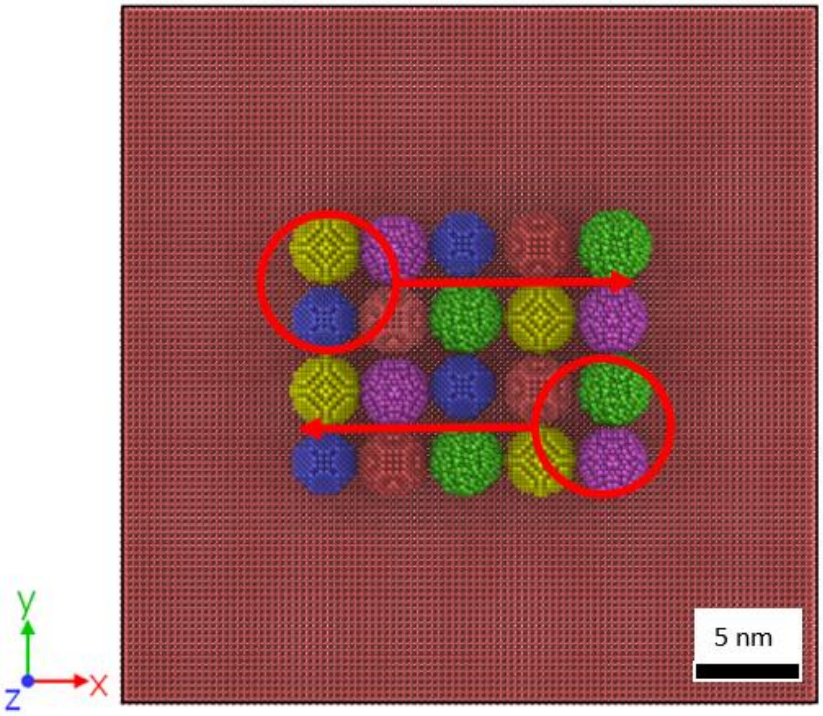

Figure 19 Initial powder bed configuration and laser pathing.

Fig. 19 shows the MSD result for two laser tracks, and it demonstrated a similar behavior as in Fig. 15, in which Mn had the highest MSD overall followed by the MSD of Co and Ni. However, there was only a marginal difference in MSD between Cr and Fe. From Fig. 20, we can also conclude that there was negligible diffusion after the initial laser interaction, the introduction of a second laser track had minimal effect on the atoms already solidifying in the previous track. Mn, Fe, and Ni were all introduced to the laser in the first track; Mn was the only element to experience notable diffusion upon the introduction of the second laser track. However, this was mainly because Mn initially melted in the first track and then filled in voids in its adjacent powders, therefore much more Mn atoms were excited by the second laser track.

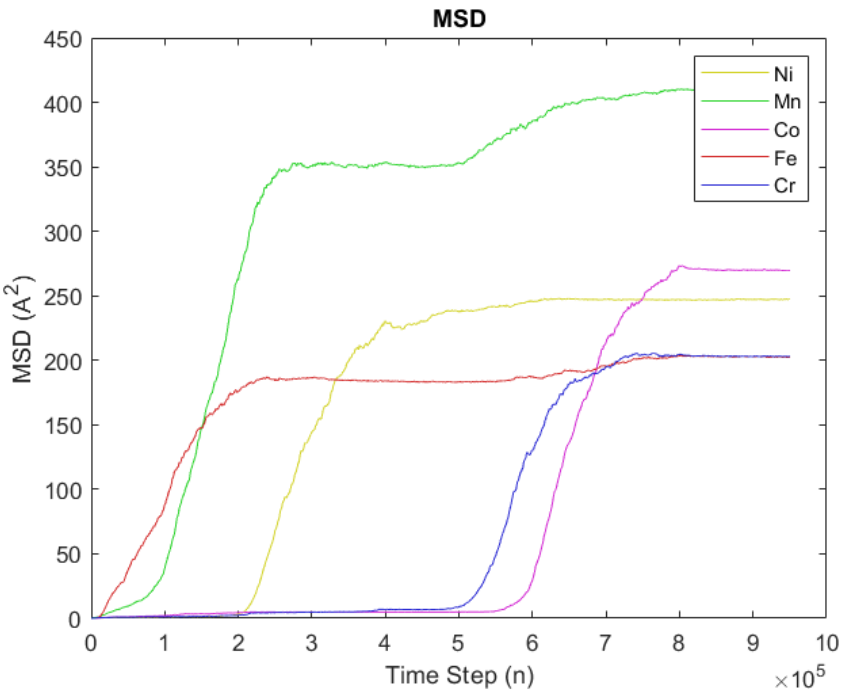

Figure 20 Mean Square Displacements of atoms selected under two subsequent tracks traveling 0.03 nm/ps

4.2.2 Multiple Track Study Composition

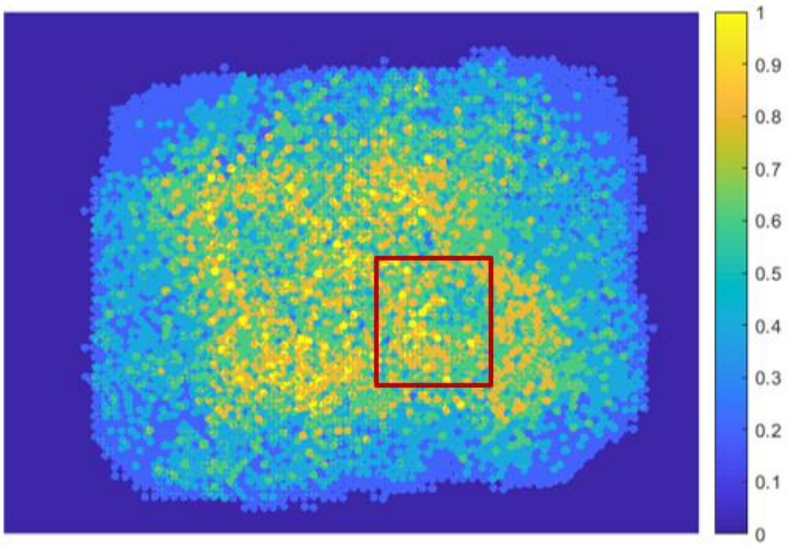

Figure 21 Pixel overlay of 2-track simulation using a meander hatch strategy.

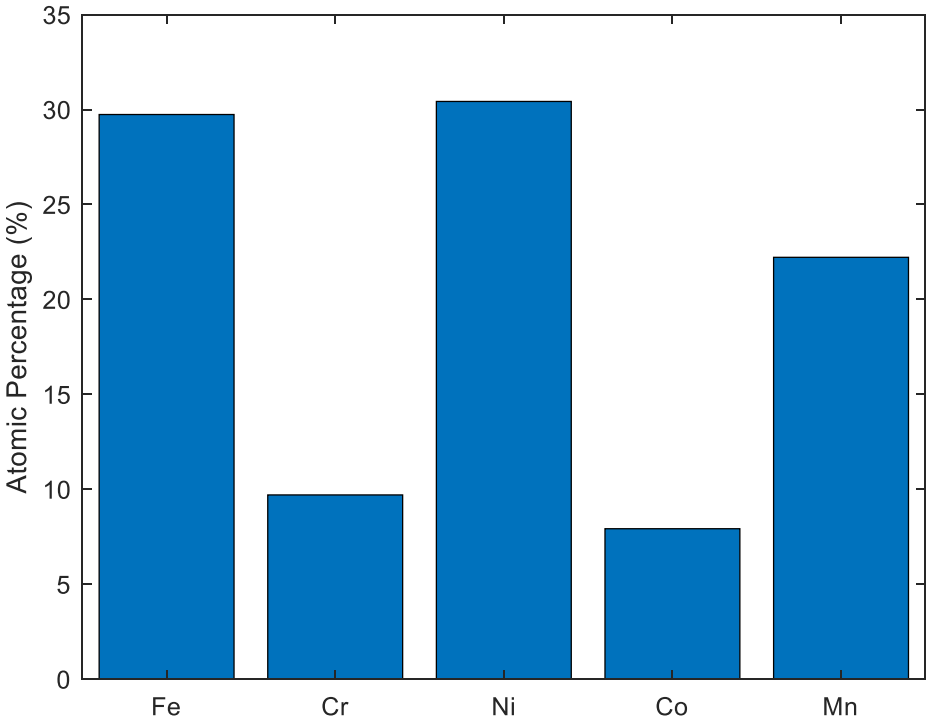

Figure 22 composition of the area indicated in fig. 21

The pixel overlay analysis in Fig. 21 shows that there was no notable increase of areas where 4 or 5 elements appeared in the final powder bed after two laser tracks. Fig. 22 further analyzes the compositions of various elements in the boxed area in Fig. 21, the areas boundaries are the same global coordinates as the area indicated in Fig. 16c. Fe, Ni, and Mn all appeared in almost identical atomic ratios, however, both Cr and Co appeared in a lower concentration, and Cr had a slightly higher concentration than Co. Given the applied two-track laser scanning strategy, many atoms, especially on the boundary of the powder bed, had more freedom to mobilize because of more laser energy input. The change in laser strategy enables different powders to interact, directly changing the composition of any given area in the powder bed.

4.2.3 Crystallization of Powder Bed

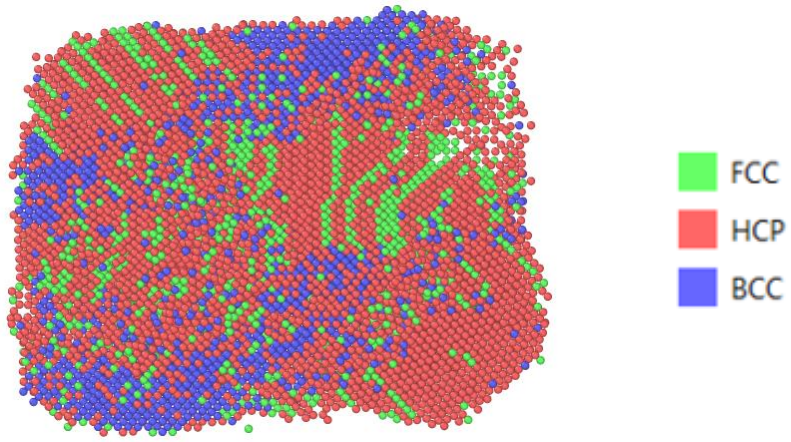

Figure 23 PTM Analysis of solidified powder bed after 2 track meander scan

Through PTM in Fig. 23, the Pure FCC crystal structure that is desired from the Co-Cr-Mn-Ni-Fe was apparent through the center of the powder bed, however, it appears as if the HCP crystal structure was dominant. Simulating with higher laser power, slower scan speed, and a more controlled cooling rate could increase the mobility of atoms in the melt pool and allow for more thorough diffusion, assuming the effects of segregation during cooling are negligible.

4.2.4 Simulation of Lattice Thermal Conductivity and Young's Modulus

- Conductivity coefficients

As mentioned in section 3.1.2, the Green-Kubo method was applied to a random solid solution Cantor alloy to verify the simulation results. From the random solid solution, the results through the temperature range of 0 K to 300 K are shown in Fig. 24.

Using the random solid solution as a control sample the results, the thermal conductivity coefficient at 300K was within 21% error when compared to experimental works (J. Yang et al., 2022). The total thermal conductivity at 300K was predicted using the Wiedemann-Franz-Lorenz relation, assuming that L = 2.45x10^-8 $W\Omega K^{-2}$ and $\rho = 1.1x10^{-6}\ \Omega m$, the electron contribution

was determined to be approximately 6.68 W/mK, the total conductivity coefficient was 9.05 W/mK; The results have an approximate error of 12% from expected results (Jin et al., 2016; J. Yang et al., 2022). There was a significant deviation from expected results at lower temperatures but given the scale of the simulation, it may be possible that Umklapp effects may increase the thermal resistivity of the lattice.

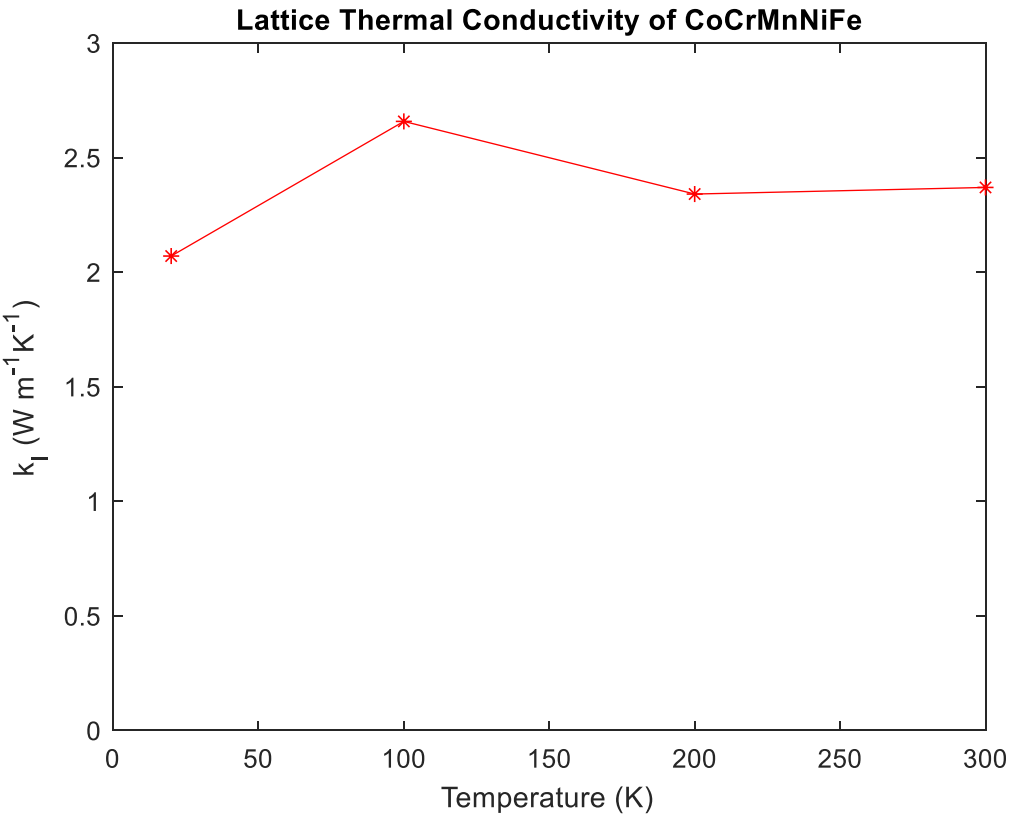

Figure 24 Lattice Thermal Conductivity of CoCrMnNiFe at 4 given temperatures

The measured lattice thermal conductivity coefficient gathered from the powder bed sample averaged about 1.99 W/mK. However, since the resultant powder bed is not homogenous, the thermal conductivity varies significantly in the x, y, and z directions. The lattice contribution is lower than what was calculated in the initial validation study, the powder bed result has many locations with varying crystal structures and compositions and the final

material lattice conductivity coefficient is much more representative of a composite conductivity coefficient of many different alloys. Moreover, the random changes in the powder bed may also contribute to phonon scattering and further reduce lattice conductivity.

- Young's and Shear Modulus

The random solid solution model calculated a Young's of modulus of 177 GPa, approximately a 12% error from experimental results published by Gludovatz et al. (2015), the model that was extracted from the powder bed exhibited lower young's modulus and shear modulus as compared to the random solid solution model. Considering that the model extracted from the powder bed is not a homogeneous Cantor HEA it is reasonable that the material properties do not match with expected results.

Table 4: Young's Modulus, Shear Modulus, Poisson's Ratio

	E (GPa)	**G (GPa)**	**Poisson ratio**
Powder Bed model	163	53	0.38
Random Solid Solution model	177	78	0.42
Gludovatz *et al.(2015)*	202	80	-

4.3 Diffusion and Entropy

- *Comparison of Diffusion Rates between Cantor alloy and Solute-Solvent based alloys*

In this study, 4 alloys were studied for diffusion coefficients, each with varying levels of Fe content: FeCoCrMnNi, Fe0.4CoCrMnNi, Fe0.6CoCrMnNi, and Fe0.8CoCrMnNi. Fig 25. Compares the diffusion coefficients of each of the given alloys at the same temperature, they are compared by their configurational entropy calculated as described in section 3.3; the alloys, their configurational entropies, and their diffusion coefficients are listed in Table 5.

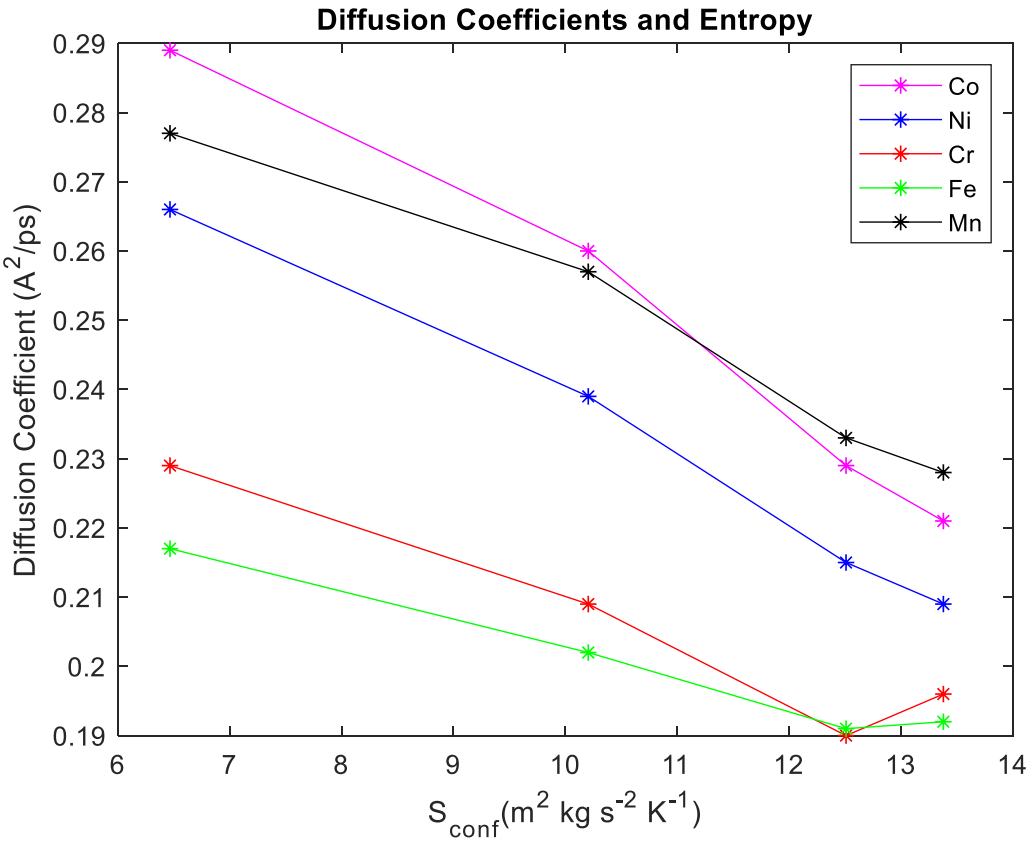

Figure 25 Diffusion Coefficients compared to Configurational Entropy, this comparison is done by comparing the alloys of increasing Fe content while maintaining equimolarity between the remaining 4 elements, proportions given in atomic percentage.

The complexity of the Cantor alloy is compared to gradually less complex alloys that resemble the more traditional solute-solvent type alloy. Fig. 25 shows that there is a general negative trend in diffusion coefficient compared to configurational entropy. This could indicate some relationship between configurational entropy and diffusion coefficient, however, the following section would suggest that the relationship is not as simple.

- *Comparison of Diffusion Rates between Cantor alloy and other Equimolar Systems*

  This study focused on three different equimolar alloys, CrNiFe, CoCrNiFe, and the

Cantor CoCrMnNiFe, in the previous study it was suggested that there may be some negative relationship between configuration entropy of a system and the diffusion rates. However, when compared to equimolar alloys with fewer principle elements, the opposite effect can be seen; Fig. 26 shows that the tracer diffusion coefficients of the Cantor HEA are significantly higher than that of the two simpler CrNiFe and CoCrNiFe systems. This behavior is not unexpected in tracer diffusion as prior works have suggested that the Cantor HEA does not exhibit "Sluggish" diffusion when compared to the equimolar CoCrNiFe (Gaertner *et al*., 2018.; Kucza *et al*., 2018).

Table 5 Diffusion Coefficients and Varying Configuration Entropy

	ΔS_conf (J/K)	**D_{Co} (Å²/ps)**	**D_{Ni} (Å²/ps)**	**D_{Cr} (Å²/ps)**	**D_{Fe} (Å²/ps)**	**D_{Mn} (Å²/ps)**
FeCoCrNiMn	13.3809	0.221	0.209	0.196	0.192	0.228
Fe0.4 CoCrNiMn	12.5108	0.229	0.215	0.190	0.191	0.233
Fe0.6CoCrNiMn	10.2057	0.260	0..239	0.209	0.202	0.257
Fe0.8CoCrNiMn	6.4655	0.289	0.266	0.229	0.217	0.277

This study may suggest that when compared to simpler equimolar alloy, there is not necessarily slower tracer diffusion due to high entropy, however, it is important to note that with the given studies this seems to only apply when the Cantor alloy is compared to other equimolar compositions; This statement does not agree with the results from the prior study when compared to systems that resemble the more traditional solute-solvent type alloy. However, it is worth noting that the first study is not exhaustive in comparing all possible alloys, i.e. alloys with Cr or Ni as solvent elements, more simulation and experiment would be needed to confirm whether the results of the first study can conclude that the Cantor HEA exhibit slower tracer diffusion than traditional alloys.

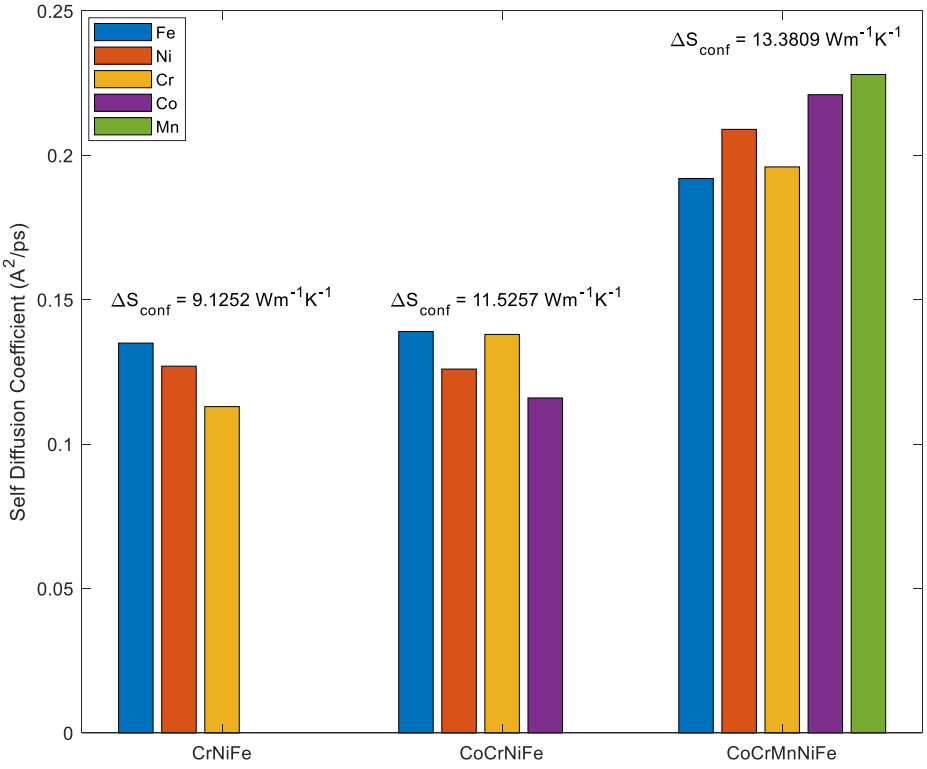

Figure 26 Diffusion Coefficients as compared to the number of components in an alloy, This study maintained equimolar ratios between the constituent elements while removing elements in each step

To relate this section to the previous sections of this thesis the results will be explained in what is expected in the LAA process and the melt pool. When comparing these alloys only, It should be expected that the CrNiFe and CoCrNiFe alloys would require higher energy density or a more carefully considered hatch strategy than needed for the Cantor HEA. From this study, there is no reason to believe that the number of principal components in an alloy system, and indirectly the entropy of the system, will slow the diffusion in the melt pool.

CHAPTER V

CONCLUSIONS AND FINDINGS

In this study, MD simulations were performed to explore the *in-situ* alloying using elemental powders, to obtain a good understanding of the effect of diffusion on the formation of Cantor HEA. The framework developed in this work can be used to explore the effect of diffusion on the thermomechanical properties of HEAs. The major findings of this study are summarized as follows:

1) All elements, when averaged, experience different MSD during the scanning process. Not only was diffusion rate different among differing elements, but active time diffusing differed as well. It may be largely influenced by the configuration of the powder bed;
2) All powders experienced the same trend in terms of MSD despite the difference in energy density introduced to the system;
3) Cr and Fe both exhibited minimal diffusion in comparison to the other constituent elements, resulting in areas where 3 or 4 elements were present in near equiatomic compositions.
4) The resulting powder bed still must be studied for its material properties and compared to the ideal alloy as well as with parts produced by prefabricated powders;
5) More work is needed to study the interdiffusion of elements in a high entropy system without the complex powder bed;

6) Per simulation, the resultant lattice conductivity coefficients calculated from the powder bed model were significantly lower than both the random solid solution model and published experimental calculations. Given the segregated powder bed the material properties were not expected to be in line with a true random solid solution;
7) As per simulation, the Young's and shear modulus were significantly lower than the results from published experimental works, this was not unexpected given the segregated powder bed.

The final study involving diffusion and entropy is a target for future work, a confirmation that the diffusion rates vary more specifically between solvent-solute type alloys and compositionally complex alloys. Further work includes studying new High Entropy Boride materials with a similar approach to observe the effects of the SLM/LAA process on material properties and their ability for application in high temperature and extreme conditions. This work can help to provide insight to what considerations must be taken into account when working with compositionally complex alloy such as HEA, and what behavior may occur in the rapid LAA process. Ultimately, this work and its subsequent works can assist the design and manufacturing of other novel HEAs for applications in extreme environment.

REFERENCES

Ahmed, S. H., & Mian, A. (2019). Influence of material property variation on computationally calculated melt pool temperature during laser melting process. *Metals*, *9*(4). https://doi.org/10.3390/MET9040456

Boltzmann, L. (1894). Zur Integration der Diffusionsgleichung bei variabeln Diffusionscoefficienten. *Annalen Der Physik*, *289*(13), 959–964. https://doi.org/10.1002/ANDP.18942891315

Butrymowicz, D. B., Manning, J. R., & Read, M. E. (1973). Diffusion in Copper and Copper Alloys. Part I. Volume and Surface Self-Diffusion in Copper. *Journal of Physical and Chemical Reference Data*, *2*(3), 643–656. https://doi.org/10.1063/1.3253129

Cantor, B., Chang, I. T. H., Knight, P., & Vincent, A. J. B. (2004). Microstructural development in equiatomic multicomponent alloys. *Materials Science and Engineering A*, *375–377*(1-2 SPEC. ISS.), 213–218. https://doi.org/10.1016/j.msea.2003.10.257

Chen, H., Fang, Q., Zhou, K., Liu, Y., & Li, J. (2020). Unraveling atomic-scale crystallization and microstructural evolution of a selective laser melted FeCrNi medium-entropy alloy. *CrystEngComm*, *22*(24), 4136–4146. https://doi.org/10.1039/d0ce00358a

Chen, W., & Zhang, L. (2017). High-Throughput Determination of Interdiffusion Coefficients for Co-Cr-Fe-Mn-Ni High-Entropy Alloys. *Journal of Phase Equilibria and Diffusion*, *38*(4), 457–465. https://doi.org/10.1007/S11669-017-0569-0

Choi, W. M., Jo, Y. H., Sohn, S. S., Lee, S., & Lee, B. J. (2018). Understanding the physical metallurgy of the CoCrFeMnNi high-entropy alloy: An atomistic simulation study. *Npj Computational Materials*, *4*(1), 1. https://doi.org/10.1038/s41524-017-0060-9

Chou, Y. L., Wang, Y. C., Yeh, J. W., & Shih, H. C. (2010). Pitting corrosion of the high-entropy alloy Co1.5CrFeNi1.5Ti0.5Mo0.1 in chloride-containing sulphate solutions. *Corrosion Science*, *52*(10), 3481–3491. https://doi.org/10.1016/j.corsci.2010.06.025

Chuang, M. H., Tsai, M. H., Wang, W. R., Lin, S. J., & Yeh, J. W. (2011). Microstructure and wear behavior of AlxCo 1.5CrFeNi1.5Tiy high-entropy alloys. *Acta Materialia*, *59*(16), 6308–6317. https://doi.org/10.1016/j.actamat.2011.06.041

Daw, M. S., & Baskes, M. I. (1983). *Semiempirical, Quantum Mechanical Calculation of Hydrogen Embrittlement in Metals*. *50*.

Dayananda, M. A., & Sohn, Y. H. (n.d.). *A New Analysis for the Determination of Ternary*

Interdiffusion Coefficients from a Single Diffusion Couple.

Ding, J., Asta, M., & Ritchie, R. O. (2018a). Melts of CrCoNi-based high-entropy alloys: Atomic diffusion and electronic/atomic structure from ab initio simulation. *Applied Physics Letters*, *113*(11). https://doi.org/10.1063/1.5045216

Divinski, S. V., Pokoev, A., Esakkiraja, N., & Paul, A. (2018). A mystery of'sluggish diffusion' in high-entropy alloys: the truth or a myth? *ArXiv*, *17*, 69–104. https://doi.org/10.4028/www.scientific.net/df.17.69

Gaertner, D., Kottke, J., Wilde, G., Divinski, S. V, & Chumlyakov, Y. (n.d.). *Tracer diffusion in single crystalline CoCrFeNi and CoCrFeMnNi high entropy alloys*. https://doi.org/10.1557/jmr.2018.162

Gao, M. C., Yeh, J.-W., Liaw, P. K., & Zhang, Y. (n.d.). *High-Entropy Alloys*.

Gludovatz, B., George, E. P., & Ritchie, R. O. (2015). Processing, Microstructure and Mechanical Properties of the CrMnFeCoNi High-Entropy Alloy. *JOM*, *67*(10), 2262–2270. https://doi.org/10.1007/S11837-015-1589-Z/FIGURES/7

Grigera, J. (2005). Molecular Dynamics Simulation for Ligand-Receptor Studies. Carbohydrates Interactions in Aqueous Solutions. *Current Pharmaceutical Design*, *8*(17), 1579–1604. https://doi.org/10.2174/1381612023394322

Hirel, P. (2015). Atomsk: A tool for manipulating and converting atomic data files. *Computer Physics Communications*, *197*, 212–219. https://doi.org/10.1016/j.cpc.2015.07.012

Hobbs, D., Hafner, J., & Spišák, D. (2003). Understanding the complex metallic element Mn. I. Crystalline and noncollinear magnetic structure of α-Mn. *Physical Review B*, *68*(1), 014407. https://doi.org/10.1103/PhysRevB.68.014407

Hou, Y., Su, H., Zhang, H., Wang, X., & Wang, C. (2021). Fabricating homogeneous fecocrni high-entropy alloys via slm in situ alloying. *Metals*, *11*(6), 942. https://doi.org/10.3390/met11060942

Hu, Y., & Li, J. (2017). Selective laser alloying of elemental titanium and boron powder: Thermal models and experiment verification. *Journal of Materials Processing Technology*, *249*, 426–432. https://doi.org/10.1016/J.JMATPROTEC.2017.06.029

Jiang, Q., Liu, H., Li, J., Yang, D., Zhang, Y., & Yang, W. (2020). Atomic-level understanding of crystallization in the selective laser melting of Fe50Ni50 amorphous alloy. *Additive Manufacturing*, *34*, 101369. https://doi.org/10.1016/j.addma.2020.101369

Jin, K., Sales, B. C., Stocks, G. M., Samolyuk, G. D., Daene, M., Weber, W. J., Zhang, Y., & Bei, H. (2016). Tailoring the physical properties of Ni-based single-phase equiatomic alloys by modifying the chemical complexity. *Scientific Reports 2016 6:1*, *6*(1), 1–10. https://doi.org/10.1038/srep20159

Kao, Y. F., Chen, T. J., Chen, S. K., & Yeh, J. W. (2009). Microstructure and mechanical property of as-cast, -homogenized, and -deformed AlxCoCrFeNi ($0 \leq x \leq 2$) high-entropy alloys. *Journal of Alloys and Compounds*, *488*(1), 57–64. https://doi.org/10.1016/J.JALLCOM.2009.08.090

Kucza, W., Dąbrowa, J., Cieślak, G., Berent, K., Kulik, T., & Danielewski, M. (2018). Studies of "sluggish diffusion" effect in Co-Cr-Fe-Mn-Ni, Co-Cr-Fe-Ni and Co-Fe-Mn-Ni high entropy alloys; determination of tracer diffusivities by combinatorial approach. *Journal of Alloys and Compounds*, *731*, 920–928. https://doi.org/10.1016/J.JALLCOM.2017.10.108

LAMMPS Molecular Dynamics Simulator. (n.d.). Retrieved April 28, 2021, from https://lammps.sandia.gov/

Lewis, L. J., Jensen, P., & Barrat, J. L. (1997). Melting, freezing, and coalescence of gold nanoclusters. *Physical Review B - Condensed Matter and Materials Physics*, *56*(4), 2248–2257. https://doi.org/10.1103/PhysRevB.56.2248

Li, R., Yuan, T., Liu, X., & Zhou, K. (2016). Enhanced atomic diffusion of Fe–Al diffusion couple during spark plasma sintering. *Scripta Materialia*, *110*, 105–108. https://doi.org/10.1016/J.SCRIPTAMAT.2015.08.012

Liu, W. H., He, J. Y., Huang, H. L., Wang, H., Lu, Z. P., & Liu, C. T. (2015). Effects of Nb additions on the microstructure and mechanical property of CoCrFeNi high-entropy alloys. *Intermetallics*, *60*, 1–8. https://doi.org/10.1016/J.INTERMET.2015.01.004

Ma, Y., Ma, Y., Wang, Q., Schweidler, S., Botros, M., Fu, T., Hahn, H., Brezesinski, T., & Breitung, B. (2021). High-entropy energy materials: challenges and new opportunities. *Energy & Environmental Science*, *14*(5), 2883–2905. https://doi.org/10.1039/D1EE00505G

MATLAB version 9.6.0.1174912 (R2019a) Update 5. (2019).

Miracle, D. B., & Senkov, O. N. (2017). A critical review of high entropy alloys and related concepts. In *Acta Materialia* (Vol. 122, pp. 448–511). Elsevier Ltd. https://doi.org/10.1016/j.actamat.2016.08.081

Montiel, H., Xu, B., & Li, J. (2019). Selective laser melting of mechanically alloyed metastable Al5Fe2 powders. *Journal of Manufacturing Science and Engineering, Transactions of the ASME*, *141*(7). https://doi.org/10.1115/1.4043730/727773

Mosallanejad, M. H., Niroumand, B., Aversa, A., & Saboori, A. (2021). In-situ alloying in laser-based additive manufacturing processes: A critical review. *Journal of Alloys and Compounds*, *872*, 159567. https://doi.org/10.1016/j.jallcom.2021.159567

Nandy, J., Yedla, N., Gupta, P., Sarangi, H., & Sahoo, S. (2019). Sintering of AlSi10Mg particles in direct metal laser sintering process: A molecular dynamics simulation study. *Materials Chemistry and Physics*, *236*, 121803. https://doi.org/10.1016/j.matchemphys.2019.121803

Pickering, E. J., Muñoz-Moreno, R., Stone, H. J., & Jones, N. G. (2016). Precipitation in the equiatomic high-entropy alloy CrMnFeCoNi. *Scripta Materialia*, *113*, 106–109. https://doi.org/10.1016/j.scriptamat.2015.10.025

Plimpton, S. (1995). Fast Parallel Algorithms for Short-Range Molecular Dynamics. In *Journal of Computational Physics* (Vol. 117). http://www.cs.sandia.gov/~sjplimp/main.html

Pranami, G., & Lamm, M. H. (2015). *Estimating Error in Diffusion Coefficients Derived from Molecular Dynamics Simulations*. https://doi.org/10.1021/acs.jctc.5b00574

Raut, J. S., Bhagat, R. B., & Fichthorn, K. A. (1998). Sintering of aluminum nanoparticles: A molecular dynamics study. *Nanostructured Materials*, *10*(5), 837–851. https://doi.org/10.1016/S0965-9773(98)00120-2

Sauer, F., & Freise, V. (1962). Diffusion in binären Gemischen mit Volumenänderung. *Zeitschrift Für Elektrochemie, Berichte Der Bunsengesellschaft Für Physikalische Chemie*, *66*(4), 353–362. https://doi.org/10.1002/BBPC.19620660412

Senkov, O. N., Wilks, G. B., Scott, J. M., & Miracle, D. B. (2011). Mechanical properties of Nb25Mo25Ta 25W25 and V20Nb20Mo 20Ta20W20 refractory high entropy alloys. *Intermetallics*, *19*(5), 698–706. https://doi.org/10.1016/j.intermet.2011.01.004

Sha, C., Zhou, Z., Xie, Z., & Munroe, P. (2020). Extremely hard, α-Mn type high entropy alloy coatings. *Scripta Materialia*, *178*, 477–482. https://doi.org/10.1016/j.scriptamat.2019.12.029

Shinoda, W., Shiga, M., & Mikami, M. (2007). *Rapid estimation of elastic constants by molecular dynamics simulation under constant stress*. https://doi.org/10.1103/PhysRevB.69.134103

Song, P., & Wen, D. (2010). Molecular dynamics simulation of the sintering of metallic nanoparticles. *Journal of Nanoparticle Research*, *12*(3), 823–829. https://doi.org/10.1007/s11051-009-9718-7

Stansbury, E. E. (Ele E., & Buchanan, R. A. (Robert A. (2000). *Fundamentals of electrochemical corrosion*. 487. https://www.researchgate.net/publication/323769144_Metallurgical_Design_of_New_Nanoporous_Structures

Stukowski, A. (2010). Visualization and analysis of atomistic simulation data with OVITO-the Open Visualization Tool. *MODELLING AND SIMULATION IN MATERIALS SCIENCE AND ENGINEERING*, *18*(1). https://doi.org/10.1088/0965-0393/18/1/015012

Torralba, J. M., Alvaredo, P., & García-Junceda, A. (2019). High-entropy alloys fabricated via powder metallurgy. A critical review. *Powder Metallurgy*, *62*(2), 84–114. https://doi.org/10.1080/00325899.2019.1584454/SUPPL_FILE/YPOM_A_1584454_SM3323.DOCX

Tsai, K. Y., Tsai, M. H., & Yeh, J. W. (2013). Sluggish diffusion in Co-Cr-Fe-Mn-Ni high-entropy alloys. *Acta Materialia*, *61*(13), 4887–4897. https://doi.org/10.1016/j.actamat.2013.04.058

Tsai, M. H. (2013). Physical properties of high entropy alloys. In *Entropy* (Vol. 15, Issue 12, pp. 5338–5345). MDPI AG. https://doi.org/10.3390/e15125338

Wakai, F. (2006). Modeling and simulation of elementary processes in ideal sintering. *Journal of the American Ceramic Society*, *89*(5), 1471–1484. https://doi.org/10.1111/j.1551-2916.2006.01001.x

Yang, J., Ren, W., Zhao, X., Kikuchi, T., Miao, P., Nakajima, K., Li, B., & Zhang, Z. (2022). Mictomagnetism and suppressed thermal conduction of the prototype high-entropy alloy CrMnFeCoNi. *Journal of Materials Science & Technology*, *99*, 55–60.

https://doi.org/10.1016/J.JMST.2021.04.077

Yang, L., Gan, Y., Zhang, Y., & Chen, J. K. (2012). Molecular dynamics simulation of neck growth in laser sintering of different-sized gold nanoparticles under different heating rates. *Applied Physics A: Materials Science and Processing*, *106*(3), 725–735. https://doi.org/10.1007/s00339-011-6680-x

Yeh, J. W., Chen, S. K., Lin, S. J., Gan, J. Y., Chin, T. S., Shun, T. T., Tsau, C. H., & Chang, S. Y. (2004). Nanostructured high-entropy alloys with multiple principal elements: Novel alloy design concepts and outcomes. *Advanced Engineering Materials*, *6*(5), 299–303. https://doi.org/10.1002/adem.200300567

Zener, C. (1951). Theory of Do for atomic diffusion in metals. *Journal of Applied Physics*, *22*(4), 372–375. https://doi.org/10.1063/1.1699967

Zhang, H., Zhao, Y., Huang, S., Zhu, S., Wang, F., & Li, D. (2019). Manufacturing and analysis of high-performance refractory high-entropy alloy via selective laser melting (SLM). *Materials*, *12*(5). https://doi.org/10.3390/ma12050720

Zhang, Y., Yang, X., & Zhang, Y. (2011). Prediction of high-entropy stabilized solid-solution in multi-component alloys Metallic glass View project High entropy alloys View project Prediction of high-entropy stabilized solid-solution in multi-component alloys. *Materials Chemistry and Physics*, *132*, 233–238. https://doi.org/10.1016/j.matchemphys.2011.11.021

Zhang, Y., Zuo, T. T., Tang, Z., Gao, M. C., Dahmen, K. A., Liaw, P. K., & Lu, Z. P. (2014). Microstructures and properties of high-entropy alloys. In *Progress in Materials Science* (Vol. 61, pp. 1–93). Elsevier Ltd. https://doi.org/10.1016/j.pmatsci.2013.10.001

Work Published by Author

This thesis was based on one conference paper and an in-progress journal paper, the author published and prepared 2020-2021.

Journal Papers (In Progress):

Farias, M., Hu, H., Zhang, S., Li, J., Xu, B.* (In Progress) Molecular Dynamic Simulations of Selective Laser Melting Process for the Cantor Alloys and its effects on Material Properties

Conference Papers:

Farias, M., Hu, H., Zhang, S., Li, J., Xu, B.* (2021, November). Molecular Dynamic Simulation of Diffusion in the Melt Pool in Laser Additive Alloying Process of Co-Ni-Cr-Mn-Fe High Entropy Alloy. ASME IMECE 2021

APPENDIX A

APPENDIX A

MOLECULAR DYNAMICS SCRIPTS USED IN THIS PAPER

Single Track Script

```
# Powder bed system with Cantor Alloy
############### DEFINE SYSTEM ##########################################
units                   metal
boundary                p p s
atom_style              atomic
read_data               HEAPB.lmp
variable        dx equal ((120/200000)*step)
region          1 block INF INF INF INF 12.9195 INF units box
region          2 block INF INF INF INF INF 12.9195 units box
region          laser cylinder z 80 143.55 30 12.9195 INF move v_dx NULL NULL
region          evap block INF INF INF INF 50 INF units box
region          Ni block 67 98.5 114 142.55 12.9195 50 units box
region          Mn block 68 97.6 144.9 171 12.9195 50 units box
region          Co block 99 126.5 114.55 142.55 12.9195 50 units box
region          Fe block 100 127.6 144.9 171 12.9195 50 units box
region          Cr block 128 153 117 142 12.9195 50 units box
pair_style              meam/c
pair_coeff * * library.meam Co Ni Cr Fe Mn CoNiCrFeMn.meam Cr Fe Ni Co Mn
neighbor                0.3 bin
neigh_modify  delay 10
velocity all create 300.0 1245532 dist gaussian rot yes units box loop geom
```

```
group Fe type 1
group Cr type 2
group Ni type 3
group Co type 4
group Mn type 5
group powder region 1
group substrate region 2
group nimsd region Ni
group mnmsd region Mn
group comsd region Co
group femsd region Fe
group crmsd region Cr
##################### ANNEAL PROCESS ###################################
# SETTING TO ROOM TEMP'
reset_timestep 0
compute                 KE all ke/atom
compute                         PE all pe/atom
fix                     1 all nvt temp 300 300 0.1
thermo                  1000
timestep                0.001
dump                    1 all atom 1000 HEAPB.lammpstrj
dump                    2 all custom 1000 HEAPB2.lammpstrj id xs ys zs c_KE c_PE fx fy
fz
run                     10000
# NVE equilibriate
```

```
unfix 1
fix                     2 all nve
fix                     3 all langevin 300 300 0.1 123432
run                     10000
unfix                   2
unfix                   3
#Start Laser
reset_timestep 0
compute                         msd1 nimsd msd com yes
compute                         msd2 mnmsd msd com yes
compute                         msd3 comsd msd com yes
compute                         msd4 femsd msd com yes
compute                         msd5 crmsd msd com yes
thermo_style            custom step c_msd1[4] c_msd2[4] c_msd3[4] c_msd4[4]
c_msd5[4]
fix                     4 substrate langevin 300 300 0.1 138182
variable                p equal 400
fix                     6 powder heat 100 v_p region laser
fix                     5 all nve
fix                     7 powder evaporate 2000 1 evap 12425132 molecule no
run                     200000
unfix 4
unfix 5
unfix 6
unfix 7
```

```
fix                     8 all nve
run                     500000
unfix 8
```

Thermal Conductivity Script

```
# input script for thermal conductivity
variable       t equal 20
variable    p equal 100    # origin 100 correlation length
variable    s equal 20     # origin 20 sample interval
variable    d equal $p*$s   # dump interval
# conversions
variable        kB equal 1.3806504e-23      # [J/K] Boltzmann
variable        eV2J equal 1.6e-19          # eV to Joule
variable        A2m equal 1.0e-10           # Angstrom to metre
variable        ps2s equal 1.0e-12          # picoseconds to s
variable        convert equal ${eV2J}*${eV2J}/${ps2s}/${A2m}
# setup problem
units                   metal
boundary                p p p
atom_style              atomic
read_data               CoNiCrFeMn.lmp
replicate               3 3 3
pair_style              meam/c
pair_coeff * * library.meam Co Ni Cr Fe Mn CoNiCrFeMn.meam Co Ni Cr Fe Mn
```

```
neighbor        0.3 bin
neigh_modify  delay 10

velocity all create $t 1545684 dist gaussian rot yes units box loop geom
group Co type 1
group Ni type 2
group Cr type 3
group Fe type 4
group Mn type 5
# 1st equilibration run
fix             1 all nvt temp $t $t 0.2
thermo          100
timestep        0.001
run             10000
velocity        all scale $t
unfix           1
# thermal conductivity calculation
reset_timestep  0
compute       myKE all ke/atom
compute       myPE all pe/atom
compute       myStress all stress/atom NULL virial
compute       flux all heat/flux myKE myPE myStress
variable      Jx equal c_flux[1]/vol
variable      Jy equal c_flux[2]/vol
variable      Jz equal c_flux[3]/vol
```

```
fix             1 all nve

fix             JJ all ave/correlate $s $p $d & c_flux[1] c_flux[2] c_flux[3] type auto & file
profile.heatflux3 ave running

variable          scale equal ${convert}/${kB}/$t/$t/vol*$s*dt

variable        k11 equal trap(f_JJ[3])*${scale}

variable        k22 equal trap(f_JJ[4])*${scale}

variable        k33 equal trap(f_JJ[5])*${scale}

thermo          $d

thermo_style    custom step temp v_Jx v_Jy v_Jz v_k11 v_k22 v_k33

run             500000

variable        kappa equal (v_k11+v_k22+v_k33)/3.0

print           "running average conductivity: ${kappa} [W/mK] @ $t K"
```

Modulus script

```
# Compute elastic constant tensor for a crystal at finite temperature

include init.mod

########## INITIAL STATES ####################

variable thermostat equal 1

include potential.mod

run ${nequil}

if "${adiabatic} == 1" &

then "variable thermostat equal 0" &
```

```
else "variable thermostat equal 1"

print ${thermostat}

include potential.mod

run ${nrun}

variable pxx0 equal f_avp[1]

variable pyy0 equal f_avp[2]

variable pzz0 equal f_avp[3]

variable pxy0 equal f_avp[4]

variable pxz0 equal f_avp[5]

variable pyz0 equal f_avp[6]

variable tmp equal lx

variable lx0 equal ${tmp}

variable tmp equal ly

variable ly0 equal ${tmp}

variable tmp equal lz

variable lz0 equal ${tmp}
```

variable d1 equal -(v_pxx1-${pxx0})/(v_delta/v_len0)*${cfac}

variable d2 equal -(v_pyy1-${pyy0})/(v_delta/v_len0)*${cfac}

variable d3 equal -(v_pzz1-${pzz0})/(v_delta/v_len0)*${cfac}

variable d4 equal -(v_pyz1-${pyz0})/(v_delta/v_len0)*${cfac}

variable d5 equal -(v_pxz1-${pxz0})/(v_delta/v_len0)*${cfac}variable d6 equal -(v_pxy1-${pxy0})/(v_delta/v_len0)*${cfac}

################ RESTART AND PERTURBATION###############################

write_restart restart.equil

uxx Perturbation

variable dir equal 1

include displace.mod

uyy Perturbation

variable dir equal 2

include displace.mod

uzz Perturbation

variable dir equal 3

include displace.mod

```
# uyz Perturbation

variable dir equal 4

include displace.mod

# uxz Perturbation

variable dir equal 5

include displace.mod

# uxy Perturbation

variable dir equal 6

include displace.mod

# Output final values

variable C11all equal ${C11}

variable C22all equal ${C22}

variable C33all equal ${C33}

variable C12all equal 0.5*(${C12}+${C21})

variable C13all equal 0.5*(${C13}+${C31})

variable C23all equal 0.5*(${C23}+${C32})
```

```
variable C44all equal ${C44}

variable C55all equal ${C55}

variable C66all equal ${C66}

variable C14all equal 0.5*(${C14}+${C41})

variable C15all equal 0.5*(${C15}+${C51})

variable C16all equal 0.5*(${C16}+${C61})

variable C24all equal 0.5*(${C24}+${C42})

variable C25all equal 0.5*(${C25}+${C52})

variable C26all equal 0.5*(${C26}+${C62})

variable C34all equal 0.5*(${C34}+${C43})

variable C35all equal 0.5*(${C35}+${C53})

variable C36all equal 0.5*(${C36}+${C63})

variable C45all equal 0.5*(${C45}+${C54})

variable C46all equal 0.5*(${C46}+${C64})

variable C56all equal 0.5*(${C56}+${C65})
```

```
##### AVERAGE MODULUS FOR CUBIC CRYSTAL ##############

variable C11cubic equal (${C11all}+${C22all}+${C33all})/3.0

variable C12cubic equal (${C12all}+${C13all}+${C23all})/3.0

variable C44cubic equal (${C44all}+${C55all}+${C66all})/3.0

variable bulkmodulus equal (${C11cubic}+2*${C12cubic})/3.0

variable shearmodulus1 equal ${C44cubic}

variable shearmodulus2 equal (${C11cubic}-${C12cubic})/2.0

variable poissonratio equal 1.0/(1.0+${C11cubic}/${C12cubic})

print "Elastic Constant C11all = ${C11all} ${cunits}"

print "Elastic Constant C22all = ${C22all} ${cunits}"

print "Elastic Constant C33all = ${C33all} ${cunits}"

print "Elastic Constant C12all = ${C12all} ${cunits}"

print "Elastic Constant C13all = ${C13all} ${cunits}"

print "Elastic Constant C23all = ${C23all} ${cunits}"

print "Elastic Constant C44all = ${C44all} ${cunits}"

print "Elastic Constant C55all = ${C55all} ${cunits}"
```

```
print "Elastic Constant C66all = ${C66all} ${cunits}"

print "Elastic Constant C14all = ${C14all} ${cunits}"

print "Elastic Constant C15all = ${C15all} ${cunits}"

print "Elastic Constant C16all = ${C16all} ${cunits}"

print "Elastic Constant C24all = ${C24all} ${cunits}"

print "Elastic Constant C25all = ${C25all} ${cunits}"

print "Elastic Constant C26all = ${C26all} ${cunits}"

print "Elastic Constant C34all = ${C34all} ${cunits}"

print "Elastic Constant C35all = ${C35all} ${cunits}"

print "Elastic Constant C36all = ${C36all} ${cunits}"

print "Elastic Constant C45all = ${C45all} ${cunits}"

print "Elastic Constant C46all = ${C46all} ${cunits}"

print "Elastic Constant C56all = ${C56all} ${cunits}"

print "Bulk Modulus = ${bulkmodulus} ${cunits}"

print "Shear Modulus 1 = ${shearmodulus1} ${cunits}"

print "Shear Modulus 2 = ${shearmodulus2} ${cunits}"
```

```
print "Poisson Ratio = ${poissonratio}"
```

Diffusion Script

```
# Example of MEAM Potential for NiCrFesystem

############### DEFINE SYSTEM ##########################################

variable th equal 3000

variable ts equal 1607

units                   metal

boundary                p p p

atom_style              atomic

read_data               FeCrNi.data

replicate       4 4 4

pair_style              meam/c

pair_coeff * * library.meam Co Ni Cr Fe Mn CoNiCrFeMn.meam Ni Cr Fe

neighbor                0.3 bin

neigh_modify  delay 10

velocity all create 300.0 1245532 dist gaussian rot yes units box loop geom

group Fe type 1
```

```
group Cr type 2

group Ni type 3

##################### ANNEAL PROCESS ###################################

# SETTING TO ROOM TEMP'

reset_timestep 0

fix                     1 all npt temp 300 300 0.1 iso 1 1 1

thermo          1000

timestep        0.001

dump            1 all atom 10000 NiCrFe_1607K.lammpstrj

run                     100000

# RAISE TEMP GRADUALLY TO HIGH TEMP

unfix 1

fix                     2 all npt temp 300 ${th} 0.1 iso 1 1 1

run                     100000

# EQUIBLIBERATE AT HIGH TEMP

unfix 2
```

```
fix                     3 all npt temp ${th} ${th} 0.1 iso 1 1 1

run                     200000

# DROP TEMP GRADUALLY TO LIQUIDUS TEMP

unfix 3

fix                     4 all npt temp ${th} ${ts} 0.1 iso 1 1 1

run                     1000000

# EQUILIBERATE AT LIQUIDUS TEMP

unfix 4

fix                     5 all npt temp ${ts} ${ts} 0.1 iso 1 1 1

run                     200000

# DATA SAMPLE WITH NVT

unfix 5

reset_timestep 0

fix                     6 all nvt temp ${ts} ${ts} 0.1

compute         msd1 Ni msd com yes

variable        twopoint1 equal c_msd1[4]/6/(step*dt+1.0e-6)
```

```
fix             msdD1 Ni vector 10 c_msd1[4]

variable        fitslope1 equal slope(f_msdD1)/6/(10*dt)

compute         msd2 Cr msd com yes

variable        twopoint2 equal c_msd2[4]/6/(step*dt+1.0e-6)

fix             msdD2 Cr vector 10 c_msd2[4]

variable        fitslope2 equal slope(f_msdD2)/6/(10*dt)

compute         msd3 Fe msd com yes

variable        twopoint3 equal c_msd3[4]/6/(step*dt+1.0e-6)

fix             msdD3 Fe vector 10 c_msd3[4]

variable        fitslope3 equal slope(f_msdD3)/6/(10*dt)

compute         msd4 all msd com yes

variable        twopoint4 equal c_msd4[4]/6/(step*dt+1.0e-6)

fix             msdD4 all vector 10 c_msd4[4]

variable        fitslope4 equal slope(f_msdD4)/6/(10*dt)

thermo_style custom step c_msd1[4] v_twopoint1 v_fitslope1 c_msd2[4] v_twopoint2
v_fitslope2 c_msd3[4] v_twopoint3 v_fitslope3 c_msd4[4] v_twopoint4 v_fitslope4 pe ke etotal
press pzz temp vol lx ly lzrun                          800000
```

BIOGRAPHICAL SKETCH

Mathew Farias attended The University of Texas Rio Grande Valley and received a Bachelor's degree in 2019. Mathew continued his education at The University of Texas Rio Grande Valley pursuing a degree in Manufacturing Engineering and finishing in the Fall of 2021 and plans to continue his academic studies pursuing a Doctorate at Mississippi State University. Mathew can be reached at: MathewFarias@gmail.com